# Journal of Turbulence

## Effects of aerodynamic interactions on the motion of heavy particles in a bidisperse suspension

PLEASE SCROLL DOWN FOR ARTICLE

# Effects of aerodynamic interactions on the motion of heavy particles in a bidisperse suspension

L.-P. WANG†∗, O. AYALA† AND W. W. GRABOWSKI‡

†Department of Mechanical Engineering, University of Delaware, Newark, DE 19716-3140, USA
‡Mesoscale and Microscale Meteorology Division, National Center for Atmospheric Research, PO Box 3000, Boulder, CO 80307-3000, USA

The effect of local aerodynamic interactions on the motion of heavy particles in a bidisperse suspension in both quiescent and turbulent air is studied by a hybrid simulation and a theoretical treatment. The particles are assumed to be small in size compared to the Kolmogorov length of the carrier air turbulence, and Stokes disturbance flows are used to represent the effect of particles. We first consider the case of no background air turbulence to validate the numerical and theoretical approaches by comparing with previous results in suspension mechanics. In a bidisperse suspension with background air turbulence, in addition to the previously known increase due to preferential sweeping, aerodynamic interactions contribute to a second augmentation in mean settling rate which depends on the flow dissipation rate. This additional increase in settling rate due to local aerodynamic interactions is also coupled with preferential concentration, in agreement with the experimental observations of Aliseda et al. (2002, *Journal of Fluid Mechanics*, **468**, 77–105). In all cases, the numerical results are explained by the theoretical approach.

*Keywords*: Particle/fluid flows; Suspensions; Turbulent flows; Sediment transport.

## 1. Introduction

The gravitational settling of particles and droplets in liquid or gas is of importance to a wide variety of applications in engineering and a host of phenomena in nature. Examples include motion of cloud droplets in the atmosphere [48], sedimentation in rivers [59], transport of pollutants [52], aggregation and deposition of pulp fibers in paper manufacturing [55] and flotation operations in ore processing [53]. In these applications, particles are usually suspended in a turbulent carrier fluid. The main objective of this paper is to present results concerning the mean settling velocity and velocity fluctuations of particles in a turbulent bidisperse suspension, specifically for the conditions relevant to cloud droplets.[1]

The sedimentation of particles in a turbulent suspension is a difficult problem because of the wide range of length and time scales that one has to consider. The carrier-fluid turbulence is typically generated and maintained by pressure gradient or mechanical stirring in engineering applications or by thermal convections and/or wind shear in the atmosphere. The integral length scale of the turbulent velocity fluctuations is usually several orders of magnitude larger than the

---

∗Corresponding author. E-mail: lwang@udel.edu

[1] The terms 'particles' and 'droplets' are used interchangeably in this paper. Cloud droplets are small and behave like solid particles as far as the viscous drag is concerned [48]. "Particles" is a more general term for other applications to which the current study may also be relevant.
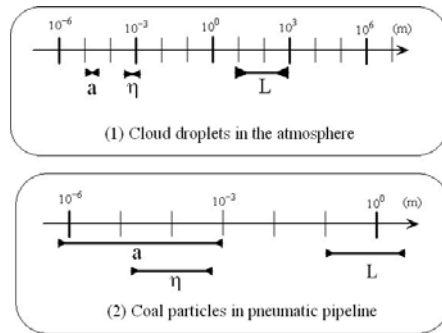
Figure 1. The relationship between different length scales in a turbulent suspension. Here *a* is the radius of particles, $\eta$ is the Kolmogorov length scale of the background turbulence, and *L* is the integral length scale of the background turbulence.

size of the particles. In figure 1, we illustrate the range of flow length scales in the problem of atmospheric cloud droplets and contrast this with a typical engineering application. A unique feature of cloud droplets is that their sizes are usually one to two orders of magnitude smaller than the Kolmogorov scale of the undisturbed or *background* air turbulence. In engineering applications, the particle size overlaps with the Kolmogorov scale.

The current study was motivated by the need to quantify the collision rates of cloud droplets in locally homogeneous atmospheric turbulence [32, 63–65], as the enhanced collision of droplets by turbulence may accelerate the initiation and development of rain drops from cloud droplets through collision-coalescence [48]. In this application, the volume fraction of droplets is typically on the order of $10^{-6}$ and the mass loading on the order of $10^{-3}$; the presence of droplets can be assumed to have little effect on the background air turbulence (i.e., one-way coupling, Elghobashi [30], Crowe et al. [21]). At the same time, the motion of a given droplet in the turbulent suspension is affected by both the background air turbulence *and* the presence of other droplets as each droplet can introduce a localized disturbance flow. Namely, the local aerodynamic interactions[2] among droplets must be considered. Given the scale separation mentioned above and the small size of the droplets, the disturbance flows will be assumed to be contained locally and dissipated quickly within Kolmogorov eddies. These assumptions make the problem of gravitational settling of cloud droplets somewhat easier to deal with, relative to a general turbulent suspension. For example, the droplet–droplet aerodynamic interactions (AI) can be approximately treated by superimposing the small-scale disturbance flows due to the droplets over the larger-scale background air turbulence [63]. Nevertheless, the inertial response time of droplets may overlap with the Kolmogorov time scale if the airflow dissipation rate is sufficiently high. This time-scale overlap can allow turbulence to modify the droplet–droplet aerodynamic interactions.

There are several consequences of the above observations. In this paper, we will demonstrate that, because of the time-scale overlap, the mean settling velocities of the droplets can be augmented by aerodynamic interactions, and this augmentation in a turbulent flow can depend on the energy dissipation rate of the turbulence and preferential concentration of droplets [1, 29, 42, 56]. Previously, without considering particle–particle aerodynamic interactions,

---

[2] The term 'aerodynamic interaction' and 'hydrodynamic interaction' are used interchangeably in this paper. Traditionally, the term 'hydrodynamic interaction' is used in the suspension mechanics to represent mutual interactions of finite-size solid particles suspended in a viscous liquid. Here in our application the fluid medium is air, therefore, "aerodynamic interaction" would be a better term. The physics of the two are identical, regardless if the carrier medium is a liquid or a gas.

Maxey [42] and Wang and Maxey [60] have shown that the settling velocity of particles can be larger than their terminal velocity due to a preferential sweeping mechanism resulting from preferential concentration of particles coupled with gravitational settling. In this paper, we will show, with both the hybrid direct numerical simulation (HDNS) approach of Wang et al. [63] and a theoretical analysis, that there is an additional increase in the mean settling velocity due to particle–particle aerodynamic interactions. This enhanced settling will be shown to depend on the volume fraction of particles, consistent with the recent experimental results of Aliseda et al. [1] who measured the settling velocity of water droplets (with diameters on the order of 10 $\mu$m) in a decaying homogeneous air turbulence. Indeed, several aspects of the experimental conditions of Aliseda et al. [1] are similar to our application. For example, the water droplets were at least one order of magnitude smaller than the flow Kolmogorov scale, with inertial response time overlapping with the flow Kolmogorov time scale. The differences in the study of Aliseda et al. [1] include a higher flow dissipation rate, a polydisperse droplet-size distribution, and a nonstationary background air turbulence. Aliseda et al. [1] found that the settling velocity of droplets increases with the volume fraction $\phi$, for $\phi$ varying from $1.5 \times 10^{-5}$ to $7 \times 10^{-5}$. In a very recent experimental study, Yang and Shy [67] measured the settling rate of solid particles in homogeneous air turbulence at a particle volume fraction of $5 \times 10^{-5}$ and found a 10–40% increase in the mean settling velocity due to interactions of particles with dissipation-range turbulent eddies, but they did not vary the volume fraction of the particles.

Another consequence is the possibility for the turbulent flow to modify the collision efficiency of droplets relative to the aerodynamic-gravitational collision efficiency. The level of this modification also depends on the level of viscous dissipation rate, and existing results are somewhat contradictory [4, 39, 47, 63].

The more general problem of average settling rate of particles in a turbulent flow when the particle size overlaps with turbulence length scales (e.g., Kolmogorov length) is a much more difficult problem. Since in that case, the turbulent carrier flow will be significantly modified by the presence of particles, the fluid motion at the particle scale has to be coupled with the evolution of turbulence at all scales. An example of an effort toward treating such a problem is the recent work of Burtin and Eaton [12, 13].

Without the background carrier-fluid turbulence, the sedimentation of particles in a suspension belongs to the topic of microhydrodynamics [37] and has been studied extensively (see review papers [25, 44, 49]). For a spherical cluster of size $L$ containing monodisperse particles settling in an unbounded fluid, the mean velocity of the particles is larger than the terminal velocity of a single particle due to hydrodynamic interactions (e.g., [34]). The particles enhance the settling motion of their surrounding particles, and the closer together they are, the stronger is the enhanced settling. Since the weight of the cluster scales as $L^3$ and the drag force scales as $L$, the fall velocity of the cluster must increase quadratically with the size of the cluster. An example of this situation is the experiment of Noh and Fernando [45]. An alternative situation is a homogeneous monodisperse suspension in an unbounded domain. Since the Stokes disturbance flow velocity decays linearly with distance, the cummulative effect of long-range hydrodynamic interactions increases quadratically with the effective interaction radius. Batchelor [5] was well aware of the divergent integrals for settling velocity. He introduced a renormalization procedure by using a frame of reference where there was no net flux (i.e., the downward flux of particle is balanced by a return fluid flow). This renormalization is essentially equivalent to introducing a mean pressure gradient to support the weight of particles, a situation similar to the sedimentation of particles in a finite-size container. Using this new reference frame, Batchelor [5] found that particles settle at a slower rate (i.e., hindered settling), and the change in the settling velocity depends linearly on the particle volume fraction when the volume fraction is low. At higher volume fraction, the change in

settling velocity may be obtained by empirical correlations based on numerous experiments (e.g., [14, 51]).

When the suspension is statistically homogeneous, theoretical predictions [15, 34] exhibit a divergent increase of the velocity fluctuations with the size of the container, with the variance of the velocity fluctuations scaled linearly with the container size and the volume fraction. The dependence of fluctuations on the container size has been demonstrated in numerical simulations where the homogeneity condition could be ensured by periodic boundary conditions [18, 41]. The theoretical prediction on fluctuations has not been supported by experiments [46], perhaps due to the fact that experimental conditions often exhibit a vertical gradient and other microstructures [43]. Several other theories based on various screening mechanisms [10, 38, 40] have also been suggested to eliminate the divergent dependence. In general, the nature of velocity fluctuations is not fully understood.

Much less is known on the sedimentation of bidisperse or polydisperse suspensions. For a homogeneous bidisperse suspension at low concentrations, Batchelor and Wen [6, 7] have derived a theory to predict the average settling velocity for each size. Their results for dilute bidisperse suspensions were later verified by experiments [3, 11, 27]. Empirical relations for sedimentation rate and stability in dense polydisperse suspensions have also been the subject of several other experimental and numerical studies [8, 19, 22, 28, 50].

In this study, we are concerned with dilute, bidisperse, non-Brownian suspensions settling in both still and turbulent air. In atmospheric clouds, a range of droplet sizes exists. Since the total volume fraction of droplets is very small, understanding the motion in a bidisperse suspension is a meaningful intermediate step toward a complete understanding of the motion of polydisperse droplets in atmospheric clouds.

The paper is organized as follows. In section 2, we describe briefly the HDNS approach [62, 63] for aerodynamically interacting particles in a turbulent flow. A theoretical approach is developed in section 3 to predict average settling velocity and velocity fluctuations. Results from HDNS will be discussed in section 4 and compared with the theoretical predictions. Finally, conclusions are provided in section 5.

## 2. The hybrid direct numerical simulation approach

This study was motivated by results from a hybrid direct numerical simulation (HDNS) approach designed for a suspension of cloud droplets whose individual motion is governed by both a dynamically evolving *background* air turbulence, generated and maintained at large scales, and local small-scale disturbance flows induced by the presence of other droplets. The droplets have a finite size and they may collide, although the percentage of droplets participated in collision is extremely small at any given time step due to the low volume fractions. The original objectives of the HDNS were to reproduce the dynamic conditions of cloud droplets in a turbulent atmosphere and to study the collision rates of aerodynamically interacting droplets in a turbulent flow [63]. For the dual purpose of understanding the methodology employed in the HDNS for such a complex system and of setting the stage for later theoretical analysis aimed at better explaining the HDNS results, we shall describe the main relevant components in HDNS.

In the context of turbulent collision of aerodynamically interacting cloud droplets, there are five components to the development of HDNS codes: (a) direct numerical simulation of *background* turbulent air flow, (b) a representation of disturbance flows due to the presence of particles, (c) tracking the motion of particles, (d) dynamic detection of collision events and post-collision treatment, and (e) computation of statistics associated with single particles and particle–particle pairs. All of these have been described in detail in our previous publications [60, 61, 63, 69], so only the essential information will be provided below.

In this paper, we focus our attention on droplets of 20–25 $\mu$m in radius, settling in air turbulence with kinetic energy dissipation rate typical of atmospheric clouds. The droplet terminal velocity is on the order of the background flow Kolmogorov velocity and the Stokes response time is typically less than the Kolmogorov time [33], turbulence–droplet interactions take place mainly in the viscous subrange and droplet–droplet aerodynamic interactions occur mainly below the Kolmogorov scale.

### 2.1 *Background air turbulence*

The air flow in core regions of cumulus clouds may be modeled as a homogeneous and isotropic turbulence by direct numerical simulations using a pseudo-spectral method. As explained in section 1, the presence of droplets has little effect on the background air turbulence which is denoted by $\mathbf{U}(\mathbf{x}, t)$. The incompressible, time-dependent and three-dimensional Navier–Stokes equations

$$\frac{\partial \mathbf{U}}{\partial t} = \mathbf{U} \times \vec{\omega} - \nabla \left( \frac{P}{\rho} + \frac{1}{2} \mathbf{U}^2 \right) + \nu \nabla^2 \mathbf{U} + \mathbf{f}(\mathbf{x}, t), \quad (1)$$

were solved along with the continuity equation $\nabla \cdot \mathbf{U} = 0$. Here $\vec{\omega} \equiv \nabla \times \mathbf{U}$ is the undisturbed air flow vorticity, $P$ is the pressure. The flow was generated from rest by the random forcing term $\mathbf{f}(\mathbf{x}, t)$ which is nonzero only for a few modes at low wavenumbers [31, 60]. After some time, the flow becomes statistically stationary when, on average, the rate of viscous dissipation at small scales balances the rate of energy addition by the forcing term at large scales.

The small-scale features of the flow are characterized by the Kolmogorov scales defined based on the viscous dissipation rate and kinematic viscosity; namely, the Kolmogorov length $\eta$, time $\tau_k$, and velocity $v_k$ are, respectively,

$$\eta = (\nu^3/\epsilon)^{1/4}, \qquad \tau_k = (\nu/\epsilon)^{1/2}, \qquad v_k = (\nu\epsilon)^{1/4}. \quad (2)$$

The large-scale features may be characterized by the r.m.s. fluctuation velocity or flow Taylor-microscale Reynolds number

$$u' \equiv \sqrt{\frac{< \mathbf{U} \cdot \mathbf{U} >}{3}}, \qquad R_\lambda = \sqrt{15} \left( \frac{u'}{v_k} \right)^2. \quad (3)$$

In HDNS, the flow Taylor-microscale Reynolds number is typically two to three orders of magnitude smaller than in real clouds, so the effects of large-scale flow features could not be directly represented in DNS. The size of the computational domain is typically on the order of 10 cm or roughly 150 $\eta$ when a $64^3$ grid and a 400 cm$^2$/s$^3$ dissipation rate are used.

### 2.2 *Disturbance flows and aerodynamic interactions*

The disturbance flows due to particles must be described for the purpose of incorporating particle–particle aerodynamic interactions. The size of the computational grid cell is typically about 2 $\eta$ which is one to two orders of magnitude larger than the radii of the particles. Figure 2 illustrates the relative length scales in HDNS. Obviously, the disturbance flows due to the particles could not be directly resolved by the computational grid used for air turbulence simulation.

What we have developed is a hybrid approach in which the disturbance flow is represented analytically. In this paper, it is assumed that the particles are very small so the disturbance flows are modeled as quasi-steady Stokes flows. An improved superposition method has recently been developed [62] in which the no-slip boundary condition on the surface of each particle
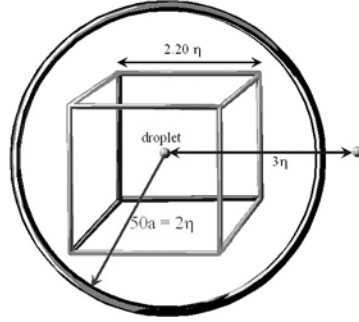
Figure 2.   Relative length scales in HDNS. The cube represents grid cell size in HDNS, the circle indicates domain of influence for aerodynamic interactions. For $64^3$ DNS at $R_\lambda = 40$, computational domain is about 141 $\eta$, grid cell size is about 2.2 $\eta$, particle diameter is 0.083 $\eta$.

is satisfied when averaged over the surface of the particle. Specifically, the fluid velocity of the composite flow at the center of each particle is equal to the velocity of that particle. This requirement leads to a more accurate representation of the force acting on a particle due to the disturbance flows by all other particles than the original superposition method (e.g., [48]).

Consider a suspension of $N_p$ particles in a background turbulent flow of velocity field $\mathbf{U}(\mathbf{x}, t)$. The composite air velocity field, after adding all the disturbance flow fields, is

$$\widetilde{\mathbf{U}}(\mathbf{x}, t) \equiv \mathbf{U}(\mathbf{x}, t) + \sum_{k=1}^{k=N_p} \mathbf{u}_s\left(\mathbf{r}^{(k)}; a^{(k)}, \mathbf{V}^{(k)} - \mathbf{U}(\mathbf{Y}^{(k)}, t) - \mathbf{u}^{(k)}\right), \tag{4}$$

where

$$\mathbf{u}_s(\mathbf{r}^{(k)}; a^{(k)}, \mathbf{V}^{(k)}) \equiv \left[\frac{3}{4}\frac{a^{(k)}}{r^{(k)}} - \frac{3}{4}\left(\frac{a^{(k)}}{r^{(k)}}\right)^3\right] \frac{\mathbf{r}^{(k)}}{(r^{(k)})^2}(\mathbf{V}^{(k)} \cdot \mathbf{r}^{(k)})$$
$$+ \left[\frac{3}{4}\frac{a^{(k)}}{r^{(k)}} + \frac{1}{4}\left(\frac{a^{(k)}}{r^{(k)}}\right)^3\right] \mathbf{V}^{(k)} \tag{5}$$

represents Stokes disturbance flow due to the $k$-th particle of radius $a^{(k)}$ moving at velocity $\mathbf{V}^{(k)}$ in an otherwise quiescent fluid, and $\mathbf{r}^{(k)} \equiv \mathbf{x} - \mathbf{Y}^{(k)}$. Here $\mathbf{Y}^{(k)}$ is the instantaneous location of the $k$-th particle. In equation (4), the combination $[\mathbf{V}^{(k)} - \mathbf{U}(\mathbf{Y}^{(k)}, t) - \mathbf{u}^{(k)}]$ represents the relative velocity between the $k$-th particle and the composite flow excluding the disturbance flow due to the $k$-th particle itself. Namely, $\mathbf{u}^{(k)}$ represents the disturbance flow velocity due to all particles except the $k$-th particle, at the location of the $k$-th particle. $\mathbf{u}^{(k)}$ is determined by applying the center-point approximation [62] to the boundary conditions $\widetilde{\mathbf{U}}(|\mathbf{r}^{(k)}| = a^{(k)}, t) = \mathbf{V}^{(k)}$, yielding

$$\mathbf{u}^{(k)} = \underbrace{\sum_{\substack{m=1 \\ m\neq k}}^{m=N_p}}_{m\neq k} \mathbf{u}_s\left(\mathbf{d}^{(mk)}; a^{(m)}, \mathbf{V}^{(m)} - \mathbf{U}(\mathbf{Y}^{(m)}, t) - \mathbf{u}^{(m)}\right), \quad \text{for} \quad k = 1, 2, \ldots, N_p, \tag{6}$$

where $\mathbf{d}^{(mk)} \equiv \mathbf{Y}^{(k)} - \mathbf{Y}^{(m)}$. The above equation represents a linear system of dimension equal to $3N_p$. We note that $\mathbf{u}^{(k)}$ is a function of both the background air flow field and the instantaneous locations and velocities of *all* particles.

Since the Stokes flow induced by $m$-th particle decays with $d^{(mk)} \equiv |\mathbf{d}^{(mk)}|$ as $a^{(m)}/d^{(mk)}$, as an approximation, we may truncate the right hand side of equation (6) if $d^{(mk)}/a^{(m)} \geq H$, or only contributions from particles in the neighborhood are considered. Physically, the dimensionless

truncation radius $H$ should be made on the order of $(\mathrm{Re}_p)^{-1}$ as the far-field disturbance flow can be better modeled by Oseen's equation [37, 45], where $\mathrm{Re}_p$ is the particle Reynolds number. Furthermore, the fluid inertial effect at the scales above the Kolmogorov scale in the turbulent background flow also implies that the Kolmogorov scale may also be a relevant scale for determining $H$. As a first step, in this paper the truncation radius $H$ is determined by a combined consideration of numerical accuracy and computational efficiency. The efficient cell-index method with cell size equal to the truncation radius and the concept of linked lists [2] were used to quickly identify all the pairs participating in aerodynamic interactions.

Once $\mathbf{u}^{(k)}$ is determined, the drag force acting on the $k$-th particle can be calculated simply as [62]

$$\mathbf{D}^{(k)} = -6\pi\mu a^{(k)}[\mathbf{V}^{(k)} - \mathbf{U}(\mathbf{Y}^{(k)}, t) - \mathbf{u}^{(k)}]. \tag{7}$$

The simulation typically involved a total of 100 000 particles, with half of the particles of size 1, and second half of size 2. The simulation considered all aerodynamic (i.e., 1–1, 1–2, 2–2) interactions, where 1–1 denotes aerodynamic interactions among size-1 particles, 1–2 denotes aerodynamic interactions of size-1 particles with size-2 particles, and 2–2 aerodynamic interactions among size-2 particles.

### 2.3 *Motion of particles*

Since the density of the droplet $\rho_p$ is much larger than the air density, the equation of motion for the $k$-th particle takes a relatively simple form

$$\frac{d\mathbf{V}^{(k)}(t)}{dt} = -\frac{\mathbf{V}^{(k)}(t) - \mathbf{U}(\mathbf{Y}^{(k)}(t), t) - \mathbf{u}^{(k)}}{\tau_p^{(k)}} - \mathbf{g}, \tag{8}$$

$$\frac{d\mathbf{Y}^{(k)}(t)}{dt} = \mathbf{V}^{(k)}(t), \tag{9}$$

where $\tau_p^{(k)} = 2\rho_p(a^{(k)})^2/(9\mu)$, $\mathbf{g}$ is the gravitational acceleration, and $\mu$ is the air viscosity. The Stokes terminal velocity of $k$-th particle is $W^{(k)} = \tau_p^{(k)}|\mathbf{g}|$.

The particles were introduced into the simulation when the background air turbulence had reached the statistically stationary stage. Then the turbulence field, disturbance flow velocities, and locations and velocities of all particles were advanced in time simultaneously. For each time step, the following procedures were implemented:

1. interpolate the undisturbed fluid velocities at the locations of the particles, $\mathbf{U}(\mathbf{Y}^{(k)}, t)$;
2. solve the disturbance velocities $\mathbf{u}^{(k)}$ using equation (6);
3. advance the velocities and locations of the particles using equations (8) and (9);
4. process collision detections, post-collision redistribution, and single particle or particle–particle pair statistics;
5. advance the undisturbed fluid turbulence field $\mathbf{U}(\mathbf{x}, t)$ using the pseudo-spectral approach.

The initial conditions were that the locations of the particles were randomly distributed and the initial velocity was set equal to the local fluid velocity plus the terminal velocity of the particle. After about $3 \times \max(\tau_{p1}, \tau_{p2})$, single-particle and particle–particle pair statistics were accumulated to obtain running averages.

The computation of the disturbance velocities or aerodynamic interactions was the most time-consuming part of the simulations, taking about 70–80% of the CPU time. The simulations were performed on NCAR's SGI Origin 3800 with 16–32 nodes and OpenMP. A typically simulation with about 4000 time steps (amounts to over 10 large-eddy turnover times) took 5–10 h of real-clock time on 32 nodes.

### 2.4  *Collision detections and post-collision treatment*

The method for collision detection went through several iterations [61, 68, 69] and the final version utilized the efficient cell-index method and the concept of linked lists [2]. A collision detection grid was carefully chosen so that all collision events were counted and, at the same time, no time was wasted on processing pairs of large separations. All collision events (1–1, 1–2, and 2–2 collisions) were considered.

No particles were allowed to overlap in space. Whenever two particles collided, they were immediately removed from their current locations and, at the same time, two new particles having the same material properties as the pair just removed were added back to the computational domain. The locations of the two new particles were randomly chosen and care was taken to make sure that they did not overlap with any other particles in the system. Their velocities were set to their terminal velocity plus the local fluid velocity. They were then tracked by solving their equation of motion just like all other particles. In this manner, the total number of particles remains the same and no particle overlaps with any other particles at the beginning of any time step. The above treatment mimics most closely the real situation of stochastic collision-coalescence of cloud droplets, since coalescence of two droplets will transform these droplets from their own size groups to a larger size group, while coalescence of smaller droplets can introduce new droplets to these size groups being considered.

A variety of statistics related to the motion of individual particles and particle–particle interactions were computed. The statistics most relevant to this study were the mean velocities of particles in all three directions and for both sizes. The pair statistics such as the radial distribution functions [57, 69] will also be needed in this study to quantify the effect of preferential concentration (e.g., [29]) on the mean motion of particles [1, 42, 60]. For further details on collision detections and computation of statistical properties, the reader is referred to Zhou et al. [68, 69].

## 3.  Theory for mean and fluctuation velocities in a bidisperse suspension

Before discussing the numerical results, we shall attempt to develop some theoretical predictions based on the setting of HDNS. These theoretical predictions provide good quantitative estimates of the effects of aerodynamic interactions on the mean and fluctuation velocities of particles. The roles of truncation radius and volume fractions of particles will also be clearly described.

### 3.1  *A model for average velocities of particles without background air turbulence*

We first consider the gravitational settling of particles in a suspension without the background air turbulence. At $t = 0$, $N^{[1]}$ particles of radius $a^{[1]}$ and known still-fluid terminal velocity $W^{[1]}$ and $N^{[2]}$ particles of radius $a^{[2]}$ and terminal velocity $W^{[2]}$ are randomly distributed in the computational domain of volume $V_{\mathrm{B}}$, with the initial velocity of each particle set to its terminal velocity. Note here we have introduced a superscript within a square brackets to represent a *group* behavior, namely, the superscript '[1]' denotes properties associated with all size-1 particles. While the superscript within parentheses such as '$(k)$', used for example in equation (8), denotes properties associated with an individual particle, i.e., the $k$-th particle. The volume fractions for the two sizes are

$$\phi^{[\alpha]} \equiv \frac{4\pi N^{[\alpha]}(a^{[\alpha]})^3}{3V_{\mathrm{B}}}, \tag{10}$$

for $\alpha = 1$ and 2. All the particles then move according to the equation of motion, equation (8), under the influence of particle inertia, Stokes drag, and gravity. The background air flow $\mathbf{U}(\mathbf{x}, t)$ is set to zero.

Without aerodynamic interactions, namely if $\mathbf{u}^{(k)}$ are all set to zero, the equation of motion has the trivial solution

$$\begin{pmatrix} V_3^{[1]}(t) \\ V_3^{[2]}(t) \end{pmatrix} = \begin{pmatrix} W^{[1]} \\ W^{[2]} \end{pmatrix}, \tag{11}$$

and the mean velocities of particles in the horizontal directions are zero. Furthermore, there are no velocity fluctuations in any direction. For convenience, we have the vertical $(3-)$ direction pointing downward to align with the direction of gravity.

The purpose here is to obtain the average behavior of particles in each size. We shall first focus on the average velocities of particles and assume that all particles in the size-1 group behaves in exactly the same manner on average and experience the same average disturbance flow velocity $u_3^{[1]}$. We shall also assume that the particles in each size-group are distributed uniformly in space. Only the mean vertical motion needs to be considered as, on average, there is no horizontal mean motion. The average equation of motion then reduces to

$$\frac{\mathrm{d}V_3^{[1]}}{\mathrm{d}t} = -\frac{\left[V_3^{[1]} - u_3^{[1]}\right]}{\tau_p^{[1]}} + g, \tag{12}$$

$$\frac{\mathrm{d}V_3^{[2]}}{\mathrm{d}t} = -\frac{\left[V_3^{[2]} - u_3^{[2]}\right]}{\tau_p^{[2]}} + g. \tag{13}$$

The question now is how to relate $u_3^{[1]}$ and $u_3^{[2]}$ to the particle velocities $V_3^{[1]}$ and $V_3^{[2]}$, concentrations $\phi^{[1]}$ and $\phi^{[2]}$, and other parameters in the numerical implementation of the aerodynamic interactions. $u_3^{[1]}$ represents the sum of all disturbance flows at the location of a size-1 particle, due to the presence of all other particles in the system. This consists of two parts: the cumulative effect of all disturbance flows due to all other size-1 particles as shown in figure 3(a)
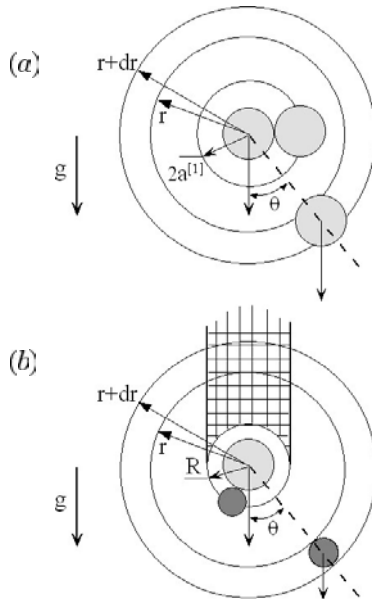


Figure 3. Sketch illustrating how the disturbance flows are summed up over spherical shells: (a) for $u_3^{[11]}$; (b) for $u_3^{[12]}$.

and the cumulative effect of all disturbance flows due to all size-2 particles as illustrated in figure 3(b). Each of these two contributions can be summed up, as shown in appendix A. A similar procedure can be used to derive $u_3^{[2]}$. Finally, $u_3^{[1]}$ and $u_3^{[2]}$ can be shown to satisfy the following linear set of equations:

$$u_3^{[1]} = 1.5\phi^{[1]}[H^2 - 4](V_3^{[1]} - u_3^{[1]}) + 1.5\phi^{[2]}f\left(H, \frac{R}{a^{[2]}}\right)(V_3^{[2]} - u_3^{[2]}), \qquad (14)$$

$$u_3^{[2]} = 1.5\phi^{[1]}f\left(H, \frac{R}{a^{[1]}}\right)(V_3^{[1]} - u_3^{[1]}) + 1.5\phi^{[2]}[H^2 - 4](V_3^{[2]} - u_3^{[2]}), \qquad (15)$$

where the function $f$ is given by Equation (A.6).

Equations (12)–(15) together completely specify the time-dependent mean motion of particles for both sizes. It is important to note that, because of the aerodynamic interactions, the motion of size-1 particles is coupled with the motion of the size-2 particles. Eliminating the disturbance flow velocities from equations (12) and (13), we can formally write

$$\begin{pmatrix} dV_3^{[1]}/dt \\ dV_3^{[2]}/dt \end{pmatrix} = \begin{pmatrix} a_{11} & a_{12} \\ a_{21} & a_{22} \end{pmatrix} \begin{pmatrix} V_3^{[1]} \\ V_3^{[2]} \end{pmatrix} + \begin{pmatrix} g \\ g \end{pmatrix}, \qquad (16)$$

again demonstrating the mean motions for two particle sizes are coupled. Here $a_{ij}$ are in general nonzero and are related to the two inertial response times $\tau_p^{[1]}$ and $\tau_p^{[2]}$, concentrations $\phi^{[1]}$ and $\phi^{[2]}$, the AI truncation radius $H$, and the particle radii $a^{[1]}$ and $a^{[2]}$.

The long-time, steady state solution is

$$\begin{pmatrix} V_3^{[1]} \\ V_3^{[2]} \end{pmatrix} = \begin{pmatrix} W^{[1]} \\ W^{[2]} \end{pmatrix} + \begin{pmatrix} 1.5\phi^{[1]}[H^2 - 4] & 1.5\phi^{[2]}f\left(H, \frac{R}{a^{[2]}}\right) \\ 1.5\phi^{[1]}f\left(H, \frac{R}{a^{[1]}}\right) & 1.5\phi^{[2]}[H^2 - 4] \end{pmatrix} \begin{pmatrix} W^{[1]} \\ W^{[2]} \end{pmatrix}. \qquad (17)$$

Since the second term on the right-hand side of the above-equation is positive, the particles settle faster, on average, than their terminal velocities. This results from the net downward disturbance flow due to all particles in the system.

It is important to recognize that the above-increased settling is computed relative to the mean motion of the *background* air turbulence. There is a nonzero mean motion of the system (i.e., particles and the air together) due to all the disturbance flows. In appendix B, we show that, if the similar renormalization procedure of Batchelor [5] is introduced, the known hindered settling of particles [5, 7] can be recovered, with coupling coefficients comparable to the classical results of Batchelor and Wen [5, 7].

## 3.2  *Velocity fluctuations without air turbulence*

Next we shall develop an approximate theoretical treatment for the long-time, r.m.s. velocity fluctuations. When a particle enters the AI truncation radius of other particles, its motion will be affected by the local disturbance flows of the other particles. Its velocity will no longer be equal to its terminal velocity in the vertical direction, and its horizontal velocities will no longer be zero. In figure 4, we show the locations from HDNS, as a function of time, in one of the horizontal directions for a pair of particles that almost collide at $t/T^{AI} = 110$. Here $T^{AI}$ is a characteristic time for aerodynamic interactions and is defined as $T^{AI} \equiv 10R/\Delta W$ with $\Delta W = |W^{[1]} - W^{[2]}|$. The average location at $t = 0$, $Y_2^{pair}(0)$, is used as the reference position, and the instantaneous location is normalized by the geometric collision radius $R$. When they almost collide at about $t/T^{AI} = 110$, both particles wobble back and forth in this horizontal direction by a distance on the order of the geometric collision radius. Also note that the smaller particle experienced two strong AI events with two other particles in the system
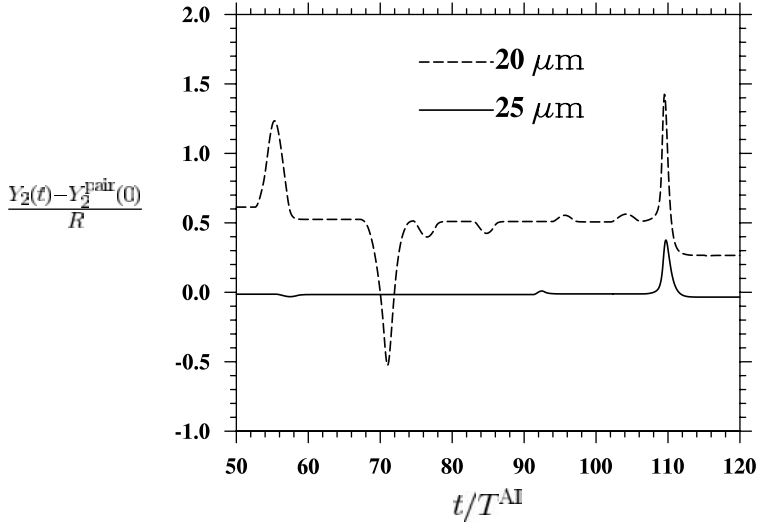
Figure 4. Locations, as function of time, in one of the horizontal directions for a pair of particles. Background air turbulence was not activated.

before that time, as shown by the two spikes at $t/T^{\mathrm{AI}} = 55$ and $t/T^{\mathrm{AI}} = 71$. There are also a few other weaker interactions between $t/T^{\mathrm{AI}} = 74$ and $t/T^{\mathrm{AI}} = 106$. All of these generate velocity fluctuations in the horizontal direction.

We first consider the velocity fluctuations in the horizontal directions. The mean velocities in the horizontal directions are zero due to the inherent symmetry of the problem. Only one of the horizontal directions needs to be considered as the r.m.s. velocity fluctuations are the same for the two horizontal directions. Assume the disturbance flow fields due to different particles are statistically uncorrelated (this is a reasonable assumption as the volume fractions are low, most of the local AI involve only two particles), then the velocity variance in the $x_2$ direction for any given size-1 particle would be the sum of the squared value of the $x_2$ component velocity of individual disturbance flows due to all other particles in the system, at the location of the size-1 particle being considered. Namely,

$$\langle (u_2^{[1]})^2 \rangle = \langle u_2^2 \rangle^{[11]} + \langle u_2^2 \rangle^{[12]}, \tag{18}$$

where $\langle u_2^2 \rangle^{[11]}$ is the velocity variance due to all other size-1 particles and $\langle u_2^2 \rangle^{[12]}$ is the velocity variance due to all size-2 particles. $\langle u_2^2 \rangle^{[11]}$ can be calculated as

$$\langle u_2^2 \rangle^{[11]} = \underbrace{\int_{2a^{[1]}}^{S^{[1]}} \mathrm{d}r \int_0^\pi \mathrm{d}\theta \int_0^{2\pi} \mathrm{d}\phi \, r^2 \sin\theta}_{\text{volume containing 1-particles involved in AI}} \times \underbrace{\frac{N^{[1]}}{V_{\mathrm{B}}}}_{\text{mean number density}}$$

$$\times \underbrace{\left[ \mathbf{u}_s(\mathbf{r}; a^{[1]}, W^{[1]}) \cdot \mathbf{e}_2 \right]^2}_{\text{contribution due to a 1-particle}}$$

$$= \int_{2a^{[1]}}^{S^{[1]}} \mathrm{d}r \int_0^\pi \mathrm{d}\theta \int_0^{2\pi} \mathrm{d}\phi \, r^2 \sin\theta \frac{N^{[1]}}{V_{\mathrm{B}}} \left\{ \left[ \frac{3}{4} \frac{a^{[1]}}{r} - \frac{3}{4} \left( \frac{a^{[1]}}{r} \right)^3 \right] W^{[1]} \sin\theta \cos\theta \cos\phi \right\}^2$$

$$= \frac{9}{80} \phi^{[1]} (W^{[1]})^2 F(H, 2), \tag{19}$$

where

$$F(H, \beta) \equiv H - \beta + \frac{2}{H} - \frac{2}{\beta} - \frac{1}{3H^3} + \frac{1}{3\beta^3}. \tag{20}$$

The expression for $\langle u_2^2 \rangle^{[12]}$ would be similar except that the range of integration for $\theta$ should exclude the shaded region in figure 3(b). However, it becomes impossible to carry out the integration analytically over such a spatial domain. Therefore, as an approximation, we choose to include the shaded region, then the final approximate expression for $\langle u_2^2 \rangle^{[12]}$ is

$$\langle u_2^2 \rangle^{[12]} \approx \frac{9}{80} \phi^{[2]} (W^{[2]})^2 F\left(H, \frac{R}{a^{[2]}}\right). \tag{21}$$

Putting all together, the r.m.s. velocity fluctuation in the horizontal direction can be approximately written as

$$\left(u_2^{[1]}\right)' \equiv \sqrt{\langle (u_2^{[1]})^2 \rangle} \approx \sqrt{\frac{9}{80} \left[ \phi^{[1]} \left(W^{[1]}\right)^2 F(H, 2) + \phi^{[2]} \left(W^{[2]}\right)^2 F\left(H, \frac{R}{a^{[2]}}\right) \right]}. \tag{22}$$

With the same level of approximation, we can obtain

$$\left(u_2^{[2]}\right)' \approx \sqrt{\frac{9}{80} \left[ \phi^{[1]} \left(W^{[1]}\right)^2 F\left(H, \frac{R}{a^{[1]}}\right) + \phi^{[2]}(W^{[2]})^2 F(H, 2) \right]}. \tag{23}$$

Similar procedure can be used to derive the velocity variance in the vertical direction. For any size-1 particle, we can write

$$\langle (u_3^{[1]})^2 \rangle = \langle u_3^2 \rangle^{[11]} + \langle u_3^2 \rangle^{[12]}, \tag{24}$$

where

$$\begin{aligned}
\langle u_3^2 \rangle^{[11]} &= \int_{2a^{[1]}}^{S^{[1]}} dr \int_0^\pi d\theta \, 2\pi r^2 \sin\theta \times \frac{N^{[1]}}{V_B} \times \left[ \mathbf{u}_s(\mathbf{r}; a^{[1]}, W^{[1]}) \cdot \mathbf{e}_3 \right]^2 \\
&= \frac{N^{[1]}}{V_B} \int_{2a^{[1]}}^{S^{[1]}} dr \int_0^\pi d\theta \, 2\pi r^2 \sin\theta \\
&\quad \times \left\{ \left[ \frac{3}{4} \frac{a^{[1]}}{r} - \frac{3}{4} \left(\frac{a^{[1]}}{r}\right)^3 \right] W^{[1]} \cos^2\theta + \left[ \frac{3}{4} \frac{a^{[1]}}{r} + \frac{1}{4} \left(\frac{a^{[1]}}{r}\right)^3 \right] W^{[1]} \right\}^2 \\
&= \frac{63}{20} \phi^{[1]} \left(W^{[1]}\right)^2 F(H, 2), \tag{25}
\end{aligned}$$

with

$$F(H, \beta) \equiv H - \beta - \frac{11}{42H} + \frac{11}{42\beta} - \frac{1}{63H^3} + \frac{1}{63\beta^3}. \tag{26}$$

Then the r.m.s. fluctuations in the vertical directions are

$$\left(u_3^{[1]}\right)' \equiv \sqrt{\langle (u_3^{[1]})^2 \rangle} \approx \sqrt{\frac{63}{20} \left[ \phi^{[1]} \left(W^{[1]}\right)^2 F(H, 2) + \phi^{[2]} \left(W^{[2]}\right)^2 F\left(H, \frac{R}{a^{[2]}}\right) \right]}, \tag{27}$$

$$\left(u_3^{[2]}\right)' \approx \sqrt{\frac{63}{20} \left[ \phi^{[1]}(W^{[1]})^2 F\left(H, \frac{R}{a^{[1]}}\right) + \phi^{[2]}(W^{[2]})^2 F(H, 2) \right]}. \tag{28}$$

These then provide theoretical estimations of the level of velocity fluctuations in the vertical direction. It differs from equations (23) and (22), for the horizontal direction.

The above predictions indicate that the velocity fluctuations are linearly proportional to the terminal velocities, the square root of volume fractions, and the square root of AI truncation radius. These are consistent with the theoretical predictions of Hinch [34] and Caflisch and Luke [15]. The above theory also predicts that the r.m.s. fluctuation velocity in the vertical direction is roughly a factor $\sqrt{28}$ (or 5.3) larger than the r.m.s. fluctuation velocity in the horizontal direction, so the fluctuation motion is strongly anisotropic.

### 3.3 *Incorporation of background air turbulence*

For simplicity, we shall only consider the quasi-steady, mean motion of particles in a turbulent flow with aerodynamic interactions. According to the equation of motion, the average velocity for the size-1 particles can be written as

$$V_3^{[1]} = W^{[1]} + \langle U_3(\mathbf{Y}^{(k)}, t) \rangle + u_3^{[1]}, \tag{29}$$

where $\langle U_3(\mathbf{Y}^{(k)}, t) \rangle$ is the average fluid velocity seen by the size-1 particles, and the average should be taken over all spatial locations occupied by size-1 particles. It is well established [42, 56, 60] that $\langle U_3(\mathbf{Y}^{(k)}, t) \rangle$ is, in general, nonzero even though the turbulent field has no mean flow (i.e., $\langle \mathbf{U}(\mathbf{x}, t) \rangle = 0$), due to the preferential sweeping resulting from the combination of preferential concentration and gravitational settling. Namely, particles are found more likely to locate themselves in regions with downward air flow, a result that has been confirmed by experiments [1, 66, 67].

We expect an additional change to the mean motion due to aerodynamic interactions, as in the case without air turbulence. This additional increase may be described by the theory developed above with a modification to take into account the non-uniform pair distribution, namely,

$$
\begin{aligned}
u_3^{[1]} &= \int_{2a^{[1]}}^{S^{[1]}} \mathrm{d}r \int_0^\pi \mathrm{d}\theta \, 2\pi r^2 \sin\theta \, g_{11}(r) \frac{N^{[1]}}{V_\mathrm{B}} \, \mathbf{u}_s(\mathbf{r}; a^{[1]}, W^{[1]}) \cdot \mathbf{e}_3 \\
&\quad \int_R^{S^{[2]}} \mathrm{d}r \int_0^\pi \mathrm{d}\theta \, 2\pi r^2 \sin\theta \, g_{12}(r) \frac{N^{[2]}}{V_\mathrm{B}} \, \mathbf{u}_s(\mathbf{r}; a^{[2]}, W^{[2]}) \cdot \mathbf{e}_3 \\
&\approx 3\phi^{[1]} W^{[1]} \int_2^H g_{11}(r) \frac{r}{a^{[1]}} \mathrm{d}\frac{r}{a^{[1]}} + 3\phi^{[2]} W^{[2]} \int_{R/a^{[2]}}^H g_{12}(r) \frac{r}{a^{[2]}} \mathrm{d}\frac{r}{a^{[2]}},
\end{aligned}
\tag{30}
$$

where $g_{11}(r)$ and $g_{12}(r)$ are radial distribution functions for 1–1 and 1–2 pairs [57, 69]. The radial distribution functions measure the effect of preferential concentration on the pair number density at separation $r = R$. In HDNS, $g_{12}$ can be computed, at any given time, as

$$g_{12}(r) = \frac{N_\mathrm{pair}/V_\mathrm{s}}{N^{[1]}N^{[2]}/V_\mathrm{B}}, \tag{31}$$

where $N_\mathrm{pair}$ is the total number of 1–2 pairs detected with separation distance falling within a thin spherical shell of average radius $r$, and $V_s$ is the volume of the spherical shell. The monodisperse radial distribution functions, $g_{11}(r)$ and $g_{22}(r)$, can be computed similarly.

The main approximation for equation (30) is the inclusion of the shaded region due to the non-overlap for the 1–2 interaction, as discussed previously. Since $g_{11}(r)$ and $g_{12}(r)$ can be larger than 1, we then expect that the additional increase in the mean velocity due to AI is larger than that without turbulence. This coupling between the preferential concentration and aerodynamic interactions is also noted in the experimental work of Aliseda et al. [1].
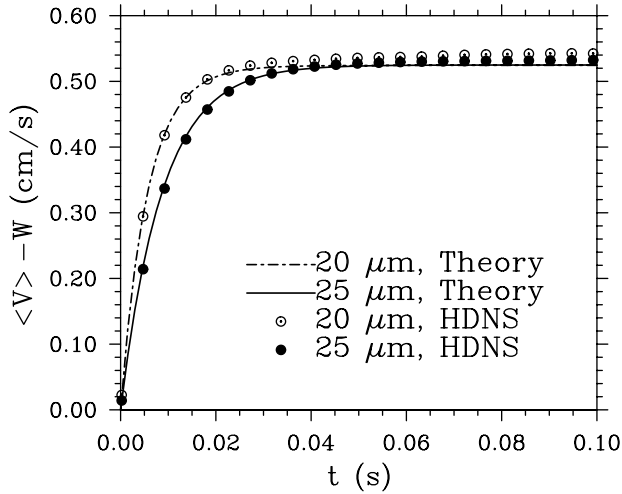
Figure 5.    The increased average settling velocities of the droplets as a function of time.

## 4.   Results and discussions

### 4.1   *Still background air*

We first discuss results without air turbulence. In figure 5, the differences between the mean velocities of the particles and their respective terminal velocity are shown for a case involving 50 000 droplets of 25 $\mu$m in radius and 50 000 droplets of 20 $\mu$m in radius in a simulation box of size equal to 6.283 *cm*. The terminal velocity and inertial response time for 25 $\mu$m droplets are 8.0147 cm/s$^{-1}$ and 0.00816 s, and those for 20 $\mu$m are 5.1294 cm/s$^{-1}$ and 0.00523 s. This corresponds to a number density of 202 cm$^{-3}$ for each size in clouds and a total liquid water content of 20.0 g/m$^3$ (or a total volume fraction of $2 \times 10^{-5}$). Since the dependence on volume fractions is known, the liquid water content was purposely made about one order of magnitude higher than in real clouds in order to show the finite effects discussed in section 3, but at a reasonable computational cost. The simulation was run for 0.9 s, only the data for the first 0.1 s were shown as we here focus on the transition to steady state. The data for $t > 0.1$ s retain the quasi-steady values. The same AI truncation radius of $H = 50$ was used in HDNS and the theory. The mean velocities increase with time initially and then reach the quasi-steady values, the relative increases are roughly the same ($\approx 0.544$ cm/s) for the two sizes, and are about 6.8% of the terminal velocity for 25 $\mu$m droplets and 10.6% of the terminal velocity for 20 $\mu$m droplets.

For the parameter setting used here, equations (14) and (15) in cm–g–s units are

$$u_3^{[1]} = 0.04939\big(V_3^{[1]} - u_3^{[1]}\big) + 0.02516\big(V_3^{[2]} - u_3^{[2]}\big), \tag{32}$$

$$u_3^{[2]} = 0.04925\big(V_3^{[1]} - u_3^{[1]}\big) + 0.02529\big(V_3^{[2]} - u_3^{[2]}\big). \tag{33}$$

Solving for $u_3^{[1]}$ and $u_3^{[2]}$ and substituting into the equations of motion, we obtain

$$\begin{pmatrix} dV_3^{[1]}/dt \\ dV_3^{[2]}/dt \end{pmatrix} = \begin{pmatrix} -116.9 & 2.869 \\ 8.763 & -186.7 \end{pmatrix} \begin{pmatrix} V_3^{[1]} \\ V_3^{[2]} \end{pmatrix} + \begin{pmatrix} 980.0 \\ 980.0 \end{pmatrix}. \tag{34}$$

It is important to note that the mean motions for the two droplet sizes are *coupled* because of the aerodynamic interactions; the degree of coupling depends on the droplet concentrations

and the AI truncation radius. The solution with the initial conditions mentioned before is

$$
\begin{pmatrix} V_3^{[1]}(t) - W^{[1]} \\ V_3^{[2]}(t) - W^{[2]} \end{pmatrix} = \begin{pmatrix} -0.5436 \\ -0.0679 \end{pmatrix} \exp\left(-\frac{t}{0.008583}\right)
$$

$$
+ \begin{pmatrix} 0.01867 \\ -0.4565 \end{pmatrix} \exp\left(-\frac{t}{0.005346}\right) + \begin{pmatrix} 0.5249 \\ 0.5244 \end{pmatrix}. \qquad (35)
$$

The coupling is further indicated by the fact that the time scales for the transient behavior of each sizes are related to the inertial response times for both sizes and the coefficients in equations (32) and (33). While the exponential coefficient in the first term is close to the inverse of $\tau_p^{(1)}$, it is not exactly the same as $1/\tau_p^{(1)}$. The exponential coefficient in the second term is also slightly different from $1/\tau_p^{(2)}$.

The above theoretical predictions are also shown in figure 5. It is remarkable that the theory predicts very well the transition to the quasi-steady state. The long-time values are also predicted well.

In figure 6, we show the long-time average mean velocities of droplets from four HDNS runs, for a bidisperse system containing $N^{[1]}$ 25 $\mu$m droplets and $N^{[2]}$ 20 $\mu$m droplets. We set $N^{[1]} = N^{[2]}$ for each run but used different total number of droplets for different runs, so four different total number concentrations are represented here. The total volume fraction is roughly the value of the total number concentration in cm$^{-3}$ multiplied by $10^{-7}$. The theoretical results from equation (17) are also shown. The theory well predicts the HDNS data, showing that the relative increases in mean settling are about the same for the two droplet sizes and are linearly dependent on the volume fraction. Aliseda et al. [1] also found experimentally that the increased settling rate increases roughly linearly with the volume fraction.

Next we show the r.m.s. velocity fluctuations in both vertical and horizontal directions for the same four runs (figure 7). In the vertical direction, the fluctuations are about the same for the two sizes and are well predicted by the theory given by equations (26) and (27), note that the two equations give almost the same result. In the horizontal direction, the HDNS data



Figure 6. The difference between the quasi-steady average settling velocity and the terminal velocity, $< V_3^{(\alpha)} > - W^{(\alpha)}$, as a function of total average number density used. The number density for each droplet size is half the total number density.
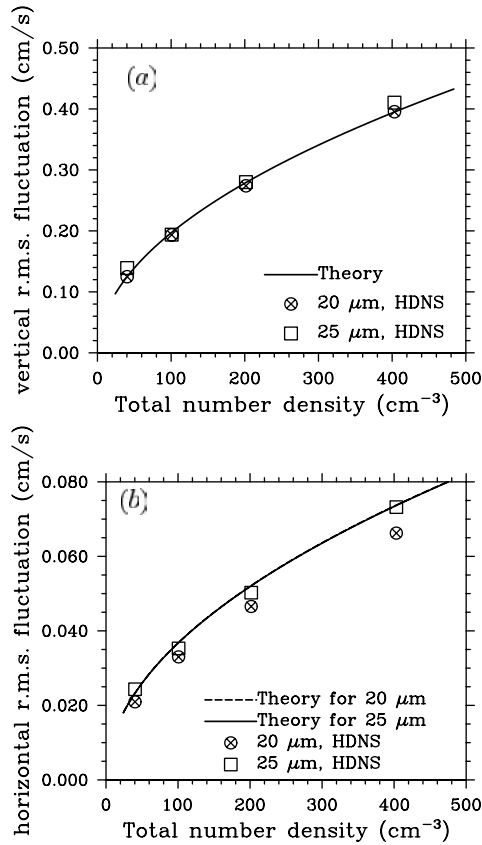
Figure 7. The r.m.s. velocity fluctuations as a function of total average number density used: (a) vertical direction, (b) horizontal direction.

show that the fluctuations for 25 $\mu$m droplets are slightly higher, while the theory based on equations (22) and (23) gives almost identical results. The theory indicates that the velocity fluctuations are proportional to the square root of number concentration, and also that the r.m.s. velocity fluctuations in the vertical direction is about 5.3 times larger than those in the horizontal direction, both well supported by the DNS results. The theory does overpredict the data in the horizontal direction, perhaps due to the inclusion of the shaded region which should be excluded due to the non-overlap condition.

Several other simulations were performed where both the AI truncation radius and the total concentration were varied, again keeping $N^{[1]} = N^{[2]}$ for each run. The results for the increased mean velocity due to AI are shown in figure 8. Again the theoretical predictions agree well with the data, showing that the relative increase is roughly proportional to $H^2$. The physical interpretation here is that, while the disturbance flow velocity decays as $O(r^{-1})$, the number of droplet pairs for AI considered increases as $O(r^3)$, leading to the net effect proportional to $H^2$. The results for the r.m.s. velocity fluctuations are displayed and compared with the theory in figure 9.

The above results consider only one size combination. In table 1, several other size combinations are considered. The simulated settling velocities are compared with the theory, showing a reasonable agreement. The difference between the theory and the simulation tends to increase with the particle volume fraction.
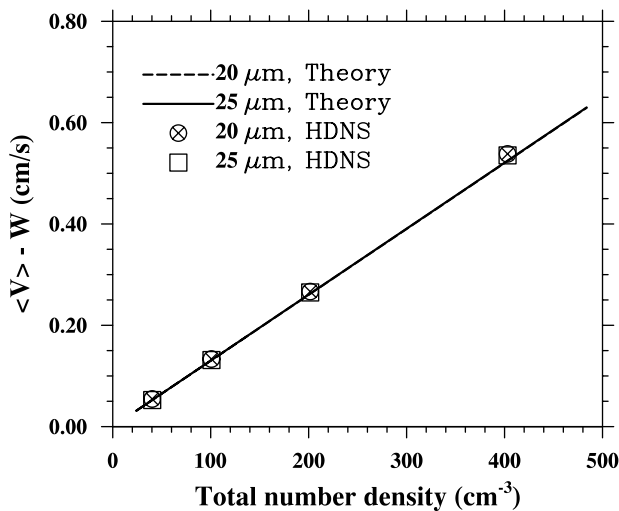
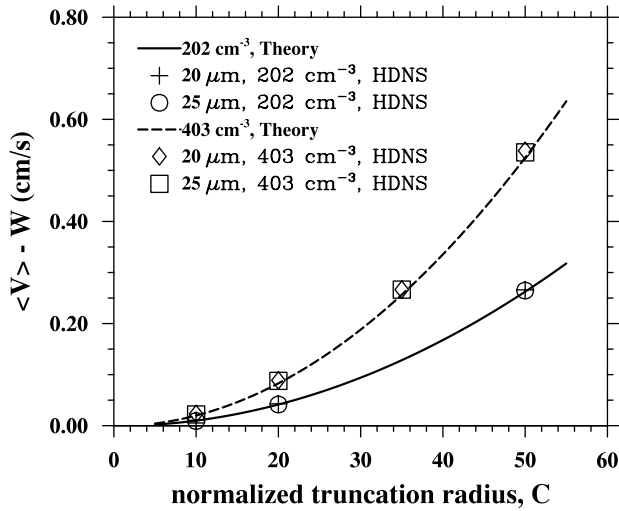Figure 8. The difference between the quasi-steady average settling velocity and the terminal velocity, $\langle V_3^{(\alpha)} \rangle - W^{(\alpha)}$, as a function of AI truncation radius. The theory essentially predicts a same value for this increase for the two sizes.
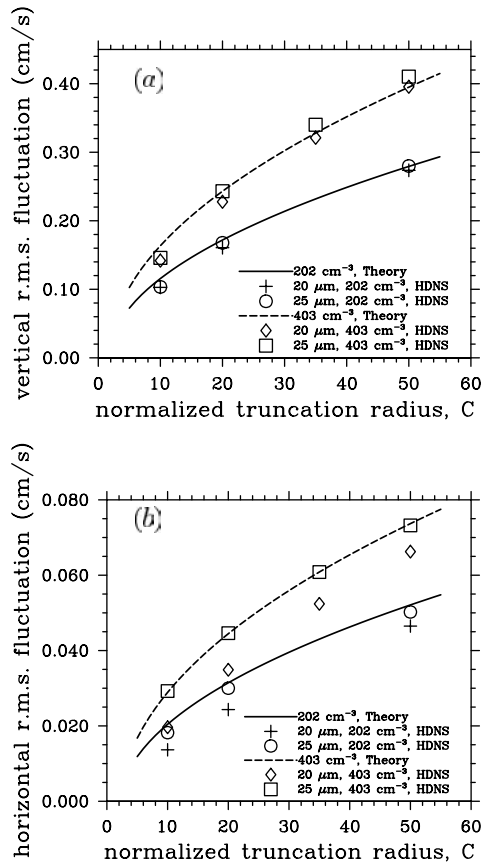


Figure 9. The r.m.s. velocity fluctuations as a function of AI truncation radius: (a) vertical direction, (b) horizontal direction.

Table 1.   Comparison of the simulated settling velocity with theory in still air, for $H = 50$

| $(a^{[1]}, a^{[2]})(\mu m)$ | (20,25) | (20,30) | (20,50) | (30,50) |
|---|---|---|---|---|
| $\phi^{[1]}$ | $4.33 \times 10^{-6}$ | $3.46 \times 10^{-6}$ | $4.33 \times 10^{-6}$ | $1.46 \times 10^{-5}$ |
| $\phi^{[2]}$ | $8.45e \times 10^{-6}$ | $1.17 \times 10^{-5}$ | $6.76 \times 10^{-5}$ | $\times 10^{-5}$ |
| $V_3^{[1]}$ (cm/s) | $5.478 \pm 0.018$ | $5.721 \pm 0.003$ | $13.421 \pm 0.004$ | $20.300 \pm 0.005$ |
| $V_3^{[2]}$ (cm/s) | $8.370 \pm 0.023$ | $12.173 \pm 0.002$ | $41.212 \pm 0.046$ | $41.973 \pm 0.041$ |
| $V_3^{[1]} - W^{[1]}$ (cm/s) | $0.348 \pm 0.018$ | $0.591 \pm 0.003$ | $8.290 \pm 0.004$ | $8.754 \pm 0.005$ |
| $V_3^{[2]} - W^{[2]}$ (cm/s) | $0.354 \pm 0.023$ | $0.631 \pm 0.002$ | $9.149 \pm 0.046$ | $9.910 \pm 0.041$ |
| $V_3^{[1]} - W^{[1]}$ (cm/s), theory | 0.336 | 0.570 | 8.189 | 8.870 |
| $V_3^{[2]} - W^{[2]}$ (cm/s), theory | 0.336 | 0.571 | 8.198 | 8.742 |

## 4.2   *Turbulent background air*

We shall now discuss selected results for the turbulent flow case. In figure 10, we display results from three runs.

(i) *Case NT-AI*. A base case with aerodynamic interactions but no air turbulence.
(ii) *Case T-NAI*. Another base case with air turbulence but no aerodynamic interactions.
(iii) *Case T-AI*. Both aerodynamic interactions and air turbulence are activated.

Again, 25 $\mu$m and 20 $\mu$m droplets are considered. The air turbulence has a dissipation rate $\epsilon = 400$ cm$^2$/s$^{-3}$. The computation domain size was 8.329 cm and 50 000 droplets were used for each size, giving volume fractions $\phi^{[1]} = 5.66 \times 10^{-6}$ and $\phi^{[2]} = 2.90 \times 10^{-6}$. The flow simulation grid was $64^3$ and the resulting Taylor microscale Reynolds number was $R_\lambda = 43.04$. The normalized AI truncation radius $H$ was 50. The Stokes numbers for the two droplet sizes are 0.396 and 0.254, while the non-dimensional terminal velocities $W/v_k$ are 2.791 and 1.786.

The long-time average statistics are shown in table 2. It is clear from both figure 10 and table 2, that the increased settling for case T-AI contains both the contribution due to the preferential sweeping (case T-NAI) and the contribution from aerodynamic interactions. The contribution due to aerodynamic interactions for case T-AI is larger than the relative increase
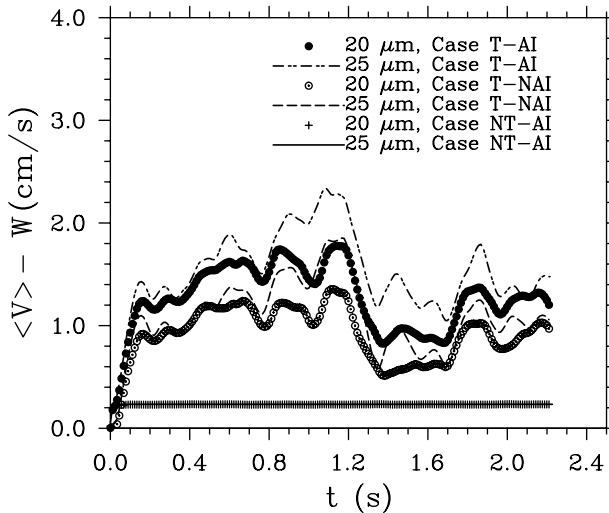


Figure 10.   The difference between the quasi-steady average settling velocity and the terminal velocity, $\langle V_3^{(\alpha)} \rangle - W^{(\alpha)}$, as a function of time for $\epsilon = 400$ cm$^2$/s$^{-3}$.

Table 2. Results for the increased settling velocities (cm/s$^{-1}$). All HDNS data were averaged over time from $t = 0.25$ s to $t = 2.20$ s. $\epsilon = 400$ cm$^2$/s$^{-3}$.

| | Case NT-AI | Case T-NAI | Case T-AI |
|---|---|---|---|
| $\langle V_3^{[1]} \rangle - W^{[1]}$: HDNS | 0.2309 | 1.0941 | 1.5226 |
| $\langle V_3^{[1]} \rangle - W^{[1]}$: theory | 0.2240 | – | – |
| $\langle V_3^{[2]} \rangle - W^{[2]}$: HDNS | 0.2315 | 0.9114 | 1.2641 |
| $\langle V_3^{[2]} \rangle - W^{[2]}$: theory | 0.2238 | – | – |
| $\sqrt{\langle (V_3^{[1]} - \langle V_3^{[1]} \rangle)^2 \rangle}$: HDNS | 0.2648 | 9.62171 | 9.63413 |
| $\sqrt{\langle (V_3^{[1]} - \langle V_3^{[1]} \rangle)^2 \rangle}$: theory | 0.2574 | – | – |
| $\sqrt{\langle (V_3^{[2]} - \langle V_3^{[2]} \rangle)^2 \rangle}$: HDNS | 0.2560 | 9.73207 | 9.73594 |
| $\sqrt{\langle (V_3^{[2]} - \langle V_3^{[2]} \rangle)^2 \rangle}$: theory | 0.2580 | – | – |

in case NT-AI, due to the preferential concentration effect, namely, the enhanced near-field pair density as quantified by the radial distribution functions.

Figure 11(a) shows the three radial distribution functions, for case T-AI, for $R^{[\alpha\beta]} < r < 10R^{[\alpha\beta]}$, where $R^{[\alpha\beta]} = a^{[\alpha]} + a^{[\beta]}$, with $\alpha, \beta = 1, 2$. We note that for this range of $r$, $g^{[12]}$ varies from 1.38 to 1.65, $g^{[11]}$ from 6.74 to 2.70, and $g^{[22]}$ varies from 3.04 to 1.96. Note that $g^{[\alpha\beta]}$ will continue to decrease with $r$ for $r > 10R^{[\alpha\beta]}$ but always be larger than 1. $g^{[11]}$ is the largest due to the larger Stokes number for 25 $\mu$m droplets [61]. $g^{[12]}$ is the smallest because droplets of different sizes tend to occupy different locations relative to small-scale flow vortical structures [69]. The different terminal velocities tend to further reduce the spatial correlation of
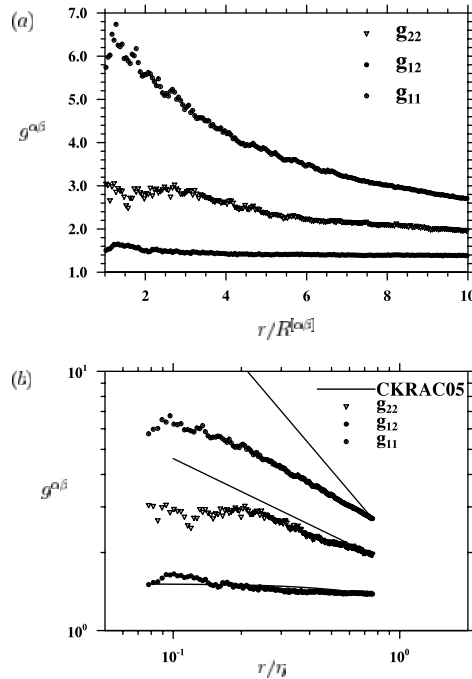


Figure 11. (a) Radial distribution functions as a function of $r/R^{[\alpha\beta]}$, where $R^{[\alpha\beta]} = a^{[\alpha]} + a^{[\beta]}$; (b) Radial distribution functions as a function of $r/\eta$ on a log-log plot. The lines represent asymptotic model predictions from Chun et al. [17].

local concentrations, and therefore the value of $g^{[12]}$. The same data are plotted in figure 11(b) on a log–log scale to compare with the recent model predictions of Chun et al. [17] who developed an asymptotic theory for the radial distribution functions of non-settling particles at small Stokes numbers, without aerodynamic interactions. For a monodisperse system, Chun et al. [17] showed that $g^{[11]}(r) \approx c_0(\eta/r)^{6.56 St^2}$ when the flow Reynolds number $R_\lambda = 47.1$ (very close to $R_\lambda = 43.04$ in our simulations here). Here $c_0$ is an unknown constant. For a bidisperse system, they showed that $g^{[12]}(r) \approx c_0[(\eta^2 + r_c^2)/(r^2 + r_c^2)]^{c_1/2}$ with $c_1 \approx 0.25$ and $r_c/\eta \approx 5(St_1 - St_2)$. Their theoretical curves are shown in figure 11(b) with the value of $c_0$ chosen to match our data at $r/R = 10$. Some evidence of the power-law scaling exists for the monodisperse radial distribution function, but with at least two deviations: (a) the power-law slope is significantly less for the larger size particles, and (b) the power-law scaling breaks down for $r/R \le 4$. The magnitudes of $g_{11}$ and $g_{22}$ level off at small separations. The shape of $g_{12}$ also appears to be more complex than the model of Chun et al. [17]. These differences could be caused by the large $St$ numbers, gravitational settling, and aerodynamic interactions that are considered here.

Using the values shown in table 2, we obtain the following relationships between the increased settling due to AI for turbulent flow and the increased settling due to AI without air turbulence:

$$\left[\langle V_3^{[1]} \rangle - W^{[1]}\right]^{\text{T}-\text{AI}} - \left[\langle V_3^{[1]} \rangle - W^{[1]}\right]^{\text{T}-\text{NAI}} = 1.856\left[\langle V_3^{[1]} \rangle - W^{[1]}\right]^{\text{NT}-\text{AI}}, \tag{36}$$

$$\left[\langle V_3^{[2]} \rangle - W^{[2]}\right]^{\text{T}-\text{AI}} - \left[\langle V_3^{[2]} \rangle - W^{[2]}\right]^{\text{T}-\text{NAI}} = 1.524\left[\langle V_3^{[2]} \rangle - W^{[2]}\right]^{\text{NT}-\text{AI}}. \tag{37}$$

The proportionality coefficients are comparable to the range of values for $g^{[\alpha\beta]}$ shown in figure 11. The proportionality coefficient for 25 $\mu$m droplets is larger than that for 20 $\mu$m, this can be explained by the fact that $g^{[11]} > g^{[22]}$.

Similarly, we could relate the increased velocity variance in the vertical direction due to AI for the turbulent flow case to the result for the no-turbulence case:

$$\langle (V_3^{[1]} - \langle V_3^{[1]} \rangle)^2 \rangle^{\text{T}-\text{AI}} - \langle (V_3^{[1]} - \langle V_3^{[1]} \rangle)^2 \rangle^{\text{T}-\text{NAI}} \approx 3.41 \langle (V_3^{[1]} - \langle V_3^{[1]} \rangle)^2 \rangle^{\text{NT}-\text{AI}},$$

$$\langle (V_3^{[2]} - \langle V_3^{[2]} \rangle)^2 \rangle^{\text{T}-\text{AI}} - \langle (V_3^{[2]} - \langle V_3^{[2]} \rangle)^2 \rangle^{\text{T}-\text{NAI}} \approx 1.15 \langle (V_3^{[2]} - \langle V_3^{[2]} \rangle)^2 \rangle^{\text{NT}-\text{AI}}.$$

Since the velocity fluctuations of droplets due to turbulent transport are much larger than the velocity fluctuations caused by AI alone, it should be noted the variances involve subtracting two large numbers so possibly a large statistical uncertainty as well. Nevertheless, the coefficients are consistent with the range of magnitude for the radial distribution functions. Again, the proportionality coefficient for 25 $\mu$m is larger due to larger $g^{[11]}$.

As yet another demonstration of the degree of coupling between AI and preferential concentration, more runs were performed at another air flow dissipation rate of 100 cm$^2$/s$^{-3}$. As before, 25 $\mu$m and 20 $\mu$m droplets were considered. The computation domain size was 11.796 cm. With 50 000 droplets for each size, the volume fractions were $\phi^{[1]} = 1.99 \times 10^{-6}$ and $\phi^{[2]} = 1.02 \times 10^{-6}$. The normalized AI truncation radius $H$ was still 50. The Stokes numbers for the two droplet sizes became 0.198 and 0.127, while the non-dimensional terminal velocities $W/v_k$ were 3.947 and 2.526. We found that

$$\left[\langle V_3 \rangle^{[1]} - W^{[1]}\right]^{\text{T}-\text{AI}} - \left[\langle V_3 \rangle^{[1]} - W^{[1]}\right]^{\text{T}-\text{NAI}} = 1.42\left[\langle V_3 \rangle^{[1]} - W^{[1]}\right]^{\text{NT}-\text{AI}}, \tag{38}$$

$$\left[\langle V_3 \rangle^{[2]} - W^{[2]}\right]^{\text{T}-\text{AI}} - \left[\langle V_3 \rangle^{[2]} - W^{[2]}\right]^{\text{T}-\text{NAI}} = 1.11\left[\langle V_3 \rangle^{[2]} - W^{[2]}\right]^{\text{NT}-\text{AI}}. \tag{39}$$

The coefficients are smaller when compared to equations (36) and (37), due to the smaller Stokes numbers and thus lower $g^{[\alpha\beta]}$ [69]. All of these demonstrate that it would be possible

Table 3. Simulated settling velocites in a turbulent air, for $H = 50$. The volume fractions are identical to the cases considered in table 1

| $(a^{[1]}, a^{[2]})(\mu\mathrm{m})$ | (20,25) | (20,30) | (20,50) | (30,50) |
|---|---|---|---|---|
| $\phi^{[1]}$ | $4.33 \times 10^{-6}$ | $3.46 \times 10^{-6}$ | $4.33 \times 10^{-6}$ | $1.46 \times 10^{-5}$ |
| $\phi^{[2]}$ | $8.45 \times 10^{-6}$ | $1.17 \times 10^{-5}$ | $6.76 \times 10^{-5}$ | $6.76 \times 10^{-5}$ |
| $(V_3^{[1]} - W^{[1]})^{\mathrm{NT-AI}}$ (cm/s) | $0.348 \pm 0.018$ | $0.591 \pm 0.003$ | $8.290 \pm 0.004$ | $8.754 \pm 0.005$ |
| $(V_3^{[2]} - W^{[2]})^{\mathrm{NT-AI}}$ (cm/s) | $0.354 \pm 0.023$ | $0.631 \pm 0.002$ | $9.149 \pm 0.046$ | $9.910 \pm 0.041$ |
| $(V_3^{[1]} - W^{[1]})^{\mathrm{T-NAI}}$ (cm/s) | $0.921 \pm 0.018$ | $0.944 \pm 0.018$ | $0.946 \pm 0.018$ | $0.835 \pm 0.027$ |
| $(V_3^{[2]} - W^{[2]})^{\mathrm{T-NAI}}$ (cm/s) | $1.105 \pm 0.023$ | $0.970 \pm 0.024$ | $0.095 \pm 0.023$ | $-0.088 \pm 0.025$ |
| $(V_3^{[1]} - W^{[1]})^{\mathrm{T-AI}}$ (cm/s) | $1.442 \pm 0.021$ | $1.658 \pm 0.020$ | $9.065 \pm 0.008$ | $9.907 \pm 0.017$ |
| $(V_3^{[2]} - W^{[2]})^{\mathrm{T-AI}}$ (cm/s) | $1.772 \pm 0.027$ | $2.217 \pm 0.032$ | $11.882 \pm 0.052$ | $12.585 \pm 0.042$ |
| $(g^{[11]})^{\mathrm{T-AI}}$ | $2.419 \pm 0.281$ | $2.112 \pm 0.267$ | $0.864 \pm 0.319$ | $2.365 \pm 0.199$ |
| $(g^{[22]})^{\mathrm{T-AI}}$ | $6.476 \pm 0.359$ | $9.398 \pm 0.406$ | $4.799 \pm 0.197$ | $4.240 \pm 0.129$ |
| $(g^{[12]})^{\mathrm{T-AI}}$ | $1.504 \pm 0.065$ | $1.220 \pm 0.050$ | $0.988 \pm 0.078$ | $1.110 \pm 0.049$ |

to predict the relative increase in settling due to AI in a turbulent flow if analytical predictions of $g^{[\alpha\beta]}$ become available and are incorporated into equation (30).

Finally, three other droplet-pair size combinations are considered and the results are compiled in Table 3. In almost all cases, the enhanced settling is the largest when both the turbulence and AI are considered. The results can be qualitatively understood with the similar reasoning presented above for the first size combination of 20 $\mu$m and 25 $\mu$m droplets.

## 5. Conclusions and Remarks

In this paper, we have investigated the motion of aerodynamically interacting particles in both turbulent and non-turbulent bidisperse suspensions. The motion of individual particles was simulated by a hybrid direct numerical simulation approach in which a three-dimensional dynamically evolving *background* air turbulence was generated and maintained at large scales, and local small-scale disturbance flows induced by the presence of other particles were imbedded analytically using an improved superposition method [62, 63]. The mean settling velocities and velocity fluctuations of particles were studied by both hybrid direct numerical simulations and by a theoretical approach. The HDNS approach does not provide an exact treatment of the near-field aerodynamic interactions [62], and should be viewed as a first step toward a rigorous treatment of turbulent dispersed flows with aerodynamically interacting particles, a subject that has never been theoretically studied previously. We have demonstrated that the HDNS can provide valuable results that can help building an improved understanding of the aerodynamic interactions on the sedimentation of bidisperse particles.

In the theoretical approach, we were able to sum up the contributions from all disturbance flows, pair by pair, over spherical shells centered on a test particle being considered. This approach was applied to bidisperse suspensions without and with background air turbulence. Both mean and fluctuation velocities have been derived, and compare well with HDNS results. Although the analysis was applied here to a bidisperse system of same density, it can be equally applied to a bidisperse system of different densities and sizes. Without air turbulence, it was found that the particles settle at a faster rate than their respective terminal velocity, relative to the undisturbed air mass in an infinite space. The relative increase is linearly dependent on the terminal velocities of the particles, the volume fractions of particles, and approximately on the squared AI truncation radius, all of which were supported by HDNS results. The theory demonstrates explicitly the coupling between the motion of two sizes within the suspension and predicts well the transition from the initial condition to the quasi-steady condition. The r.m.s.

velocity fluctuations were also successfully predicted by the theory. The observed velocity fluctuations imply that the collision efficiencies between droplets in atmospheric clouds could depend on the presence of all other droplets in the suspension. We note that, although the mean velocity of the particles depends on the truncation radius, the relative motion of particles is not sensitive to the truncation radius, as shown in Wang et al. [63].

When the normalization of Batchelor [5] is applied or the mean motion of the full system due to all the disturbances are subtracted out, then the particles settle at a slower velocity than their respective terminal velocity, consistent with the theory of hindered settling [5, 7]. We also demonstrate that the sedimentation coefficients in a bidisperse system vary greatly depending on the size ratio, in qualitative agreement with the theoretical results of Batchelor and Wen [6, 7]. Our study also reveals the need to further improve the superposition method for near-field interactions to obtain better quantitative results of sedimentation rates. The theoretical result for the velocity fluctuation is consistent with previous results for homogeneous suspensions [15, 34], and shows a strong anisotropy of the fluctuation motion.

In a turbulent suspension, particles of finite inertia can settle faster than their terminal velocities for two reasons. First, the preferential sweeping effect [60] biases the trajectories of particles toward regions with downward local air velocity due to the combined effect of preferential concentration and gravitational settling. Second, the aerodynamic interactions by the disturbance flows introduce net downward velocity on particles. Here we demonstrated, both numerically and theoretically, that the additional increased settling due to the AI was also augmented by the preferential concentration effect which depends on the dissipation rate of the background air turbulence. The observed coupling between aerodynamic interactions and preferential concentration as well as its effect on the sedimentation rate in a turbulent flow are consistent with the experimental results of Aliseda et al. [1].

The assumption of Stokes disturbance flows used in this study is invalid in the far field, implying that the theory becomes inaccurate as the AI truncation radius grows. In reality, for any given particle Reynolds number $Re_p$, no matter how small it may be, the Stokes disturbance flow due to a particle of radius $a$, will break down at a distance larger than $r > aRe_p^{-1}$ [37]. In other words, the far-field disturbance flow should decay faster than $O(r^{-3})$ so the integrals might converge if the AI truncation radius is increased indefinitely. The cumulative long-range aerodynamic interactions [54] further accelerate the finite-Reynolds number effect; the same argument applies to a cluster of particles as the size of cluster grows [45]. On the other hand, since the results remain qualitatively the same for different AI truncation radii, we expect that the results illustrated in this paper be qualitatively valid for a wider range of particle Reynolds numbers. The screening mechanism related to the fluid inertia [10, 38, 40] implies that, if the inter-particle separation is larger than the flow Kolmogorov scale, the truncation radius will depend on the flow Kolmogorov scale. We speculate that, for a dilute turbulent suspension considered in our paper, the truncation radius will depend on both the particle size and the flow Kolmogorov scale, the exact nature of these dependences is a topic for future research.

The results presented in this paper should be viewed as a first step toward a better understanding of the sedimentation in turbulent suspension for atmospheric cloud droplets and other related applications. When scaled with the realistic mass loading or liquid water content (i.e., $1\,\mathrm{g/m}^{-3}$) in atmospheric clouds, the relative increase in the settling rate is about 2%–3% and should be viewed as a small change. Since there is a distinct difference in the Reynolds number between the HDNS airflow and the atmospheric turbulence, the question of whether this change increases with flow Reynolds number should be studied in the future. This Reynolds number dependence is related to the issue of the Reynolds number dependence of the radial distribution function (e.g., [20]). The results of Yang and Shy [67] on the increased settling rate of solid particles in turbulent air appear to suggest a strong flow Reynolds number dependence. In engineering applications where the volume fractions of droplets and flow dissipation

rates are much higher, the level of increase in the settling rate could be much more significant [1, 67]. For example, in the experiments of Aliseda et al. [1] the flow dissipation rates are one to two orders of magnitude higher. Under a similar level of volume fractions, Alidesa et al. [1] found a much higher level of increased settling. The underlying mechanisms are essentially the same as these discussed in this paper, and the theoretical predictions developed here appear to provide a better understanding of their observations. A direct comparison with the data of Aliseda et al. [1] would require a further parametric study of the turbulent sedimentation for different droplet size combinations and flow dissipation rates as well as the use of a poly-disperse size distribution. Given the level of the particle volume fraction ($5 \times 10^{-5}$) in the study of Yang and Shy [67], we speculate that part of the significant increase in the settling velocity of solid particles in turbulent air, that they observed experimentally, could be due to the aerodynamic interactions discussed in this paper.

Finally, we note that analytical and numerical methods using Stokesian dynamics simulations, multipole techniques at large separations, and lubrication expansion for small separations [9,16,24,36] are the logical next step to improve our approach. When the minimum separation between two particles approaches the mean free path of fluid medium, non-continuum effects [35, 58] also need to be considered. The recent work by Chun and Koch [16] is particularly relevant in this regard.

### Acknowledgements

### Appendices

### A. Appendix Derivations of average disturbance motion, $u_3^{[1]}$ and $u_3^{[2]}$

The cummulative effect of all disturbance flows at the location of a size-1 particle can be decomposed as

$$u_3^{[1]} = u_3^{[11]} + u_3^{[12]}, \tag{A.1}$$

where $u_3^{[11]}$ denotes the sum of all disturbance flows due to all other size-1 particles located within a radius of $S^{[1]} \equiv Ha^{[1]}$ from the size-1 particle being considered and is given as

$$u_3^{[11]} = \underbrace{\int_{2a^{[1]}}^{S^{[1]}} dr \int_0^\pi d\theta\, 2\pi r^2 \sin\theta}_{\text{volume containing 1-particles involved in AI}} \times \underbrace{\frac{N^{[1]}}{V_B}}_{\text{mean number density}} \times \underbrace{\mathbf{u}_s(\mathbf{r}; a^{[1]}, (V_3^{[1]} - u_3^{[1]})\mathbf{e}_3) \cdot \mathbf{e}_3}_{\text{contribution due to a 1-particle}}.$$

$$\tag{A.2}$$

Here $H$ is the normalized AI truncation radius. In writing the above equation, the contributions are summed over infinitesimal spherical shells (figure 3a). Physical interpretations of the different parts in the above equation are indicated by the text underneath them. Substituting

the expression for the Stokes disturbance flow $\mathbf{u}_s$ as given by equation (5), we obtain

$$u_3^{[11]} = 1.5\phi^{[1]} \left[ \left( \frac{S^{[1]}}{a^{[1]}} \right)^2 - 4 \right] \left( V_3^{[1]} - u_3^{[1]} \right). \tag{A.3}$$

Similarly, $u_3^{[12]}$ denotes the sum of disturbance flows due to all size-2 particles located with a radius of $S^{[2]} \equiv Ha^{[2]}$ from the size-1 particle being considered. $u_3^{[12]}$ can be expressed as

$$u_3^{[12]} = \underbrace{\int_{R=a^{[1]}+a^{[2]}}^{S^{[2]}} dr \int_0^{\pi - \sin^{-1}\frac{R}{r}} d\theta \, 2\pi r^2 \sin\theta}_{\text{accessible volume to 2-particles involved in AI}} \times \quad \underbrace{\frac{N^{[2]}}{V_B}}_{\text{mean number density}}$$

$$\times \underbrace{\mathbf{u}_s \left( \mathbf{r}; a^{[2]}, \left( V_3^{[2]} - u_3^{[2]} \right) \mathbf{e}_3 \right) \cdot \mathbf{e}_3}_{\text{contribution due to a 2-particle}}. \tag{A.4}$$

Here the range of integration over the polar angle $\theta$ is modified due to the non-overlap condition (figure 3b) which is discussed in detail in [63]. The shaded region in figure 3b indicates the region where no size-2 particles are found relative to the size-1 particle considered. Performing the integration with the Stokes disturbance flow gives

$$u_3^{[12]} = 1.5\phi^{[2]} f \left( \frac{S^{[2]}}{a^{[2]}}, \frac{R}{a^{[2]}} \right) \left( V_3^{[2]} - u_3^{[2]} \right), \tag{A.5}$$

where

$$f(\alpha, \beta) = 0.5(\alpha^2 - \beta^2) + 0.75\alpha\sqrt{\alpha^2 - \beta^2}$$
$$- 0.25 \left( \frac{1}{\alpha} - \frac{1}{3\alpha^3} \right) (\alpha^2 - \beta^2)^{1.5} - 0.75\beta^2 \cosh^{-1} \left( \frac{\alpha}{\beta} \right). \tag{A.6}$$

To be complete, we should note that the above equation applies when $\alpha > \beta$. If $\alpha \leq \beta$ or $S^{[2]} \leq R$ which means that the radius of size-1 particles is much larger than the radius of size-2 particles such that it is impossible to find the center of any size-1 particle being within the AI truncation radius from any size-2 particle, then $f(\alpha, \beta) = 0$.

When $H \gg R/a^{[2]}$, we have

$$f \left( \frac{S^{[2]}}{a^{[2]}}, \frac{R}{a^{[2]}} \right) \approx \left( \frac{S^{[2]}}{a^{[2]}} \right)^2. \tag{A.7}$$

Therefore, for very large AI truncation radius, both equations (A.7) and (A.3) indicate that the effect of aerodynamic interaction increases with the square of the truncation radius, implying that the integrals represented by equations (A.2) and (A.4) will not converge if the truncation radii are made indefinite. This property has been noted, for example, by Batchelor [5], and is due to the very slow decay (i.e., $O(r^{-1})$) of the Stokes disturbance flow at large distance.

A similar procedure can be used to derive $u_3^{[2]}$. Putting all together, the average cumulative disturbance flow magnitudes can be solved by the following linear set of equations:

$$u_3^{[1]} = 1.5\phi^{[1]}[H^2 - 4] \left( V_3^{[1]} - u_3^{[1]} \right) + 1.5\phi^{[2]} f \left( H, \frac{R}{a^{[2]}} \right) \left( V_3^{[2]} - u_3^{[2]} \right), \tag{A.8}$$

$$u_3^{[2]} = 1.5\phi^{[1]} f \left( H, \frac{R}{a^{[1]}} \right) \left( V_3^{[1]} - u_3^{[1]} \right) + 1.5\phi^{[2]}[H^2 - 4] \left( V_3^{[2]} - u_3^{[2]} \right). \tag{A.9}$$

**Appendix B. A renormalization to recover the hindered settling**

The increased settling discussed in section 3.1 is computed relative to the mean motion of the *background* air turbulence. There is a nonzero mean motion of the system (i.e., particles and the air together) due to all the disturbance flows, assuming that no external inverse pressure gradient exists to counter balance the mean motion. This total mean motion at the long-time, quasi-steady stage can be written as

$$u_3^{[fp]} = u_3^{[fp1]} + u_3^{[fp2]}, \tag{B.1}$$

where the superscript $[fp]$ denotes all space occupied by both the fluid and the particles. Here $u_3^{[fp1]}$ denotes all contributions due to size-1 particles and can be expressed as

$$u_3^{[fp1]} = \underbrace{\frac{1}{V_B} \int_{a^{[1]}}^{S^{[1]}} dr \int_0^{\pi} d\theta\, 2\pi r^2 \sin\theta\, \mathbf{u}_s(\vec{r}; a_1, W^{[1]}\mathbf{e}_3) \cdot \mathbf{e}_3 \times N^{[1]}}_{\text{contribution due to flow outside a single 1-particle}}$$

$$+ \underbrace{\phi^{[1]}\big(W^{[1]} + u_3^{[1]}\big),}_{\text{contribution due to 1-particles within their own space}} \tag{B.2}$$

yielding

$$u_3^{[fp1]} = 1.5\phi^{[1]}\big[H^2 - 1\big] W^{[1]} + \phi^{[1]}\big(W^{[1]} + u_3^{[1]}\big). \tag{B.3}$$

A similar expression can be obtained for $u^{[fp2]}$. Therefore,

$$u_3^{[fp]} = (1.5H^2 - 0.5)\big(\phi^{[1]}W^{[1]} + \phi^{[2]}W^{[2]}\big) + \phi^{[1]}u_3^{[1]} + \phi^{[2]}u_3^{[2]}. \tag{B.4}$$

The last two terms on the right-hand side may be neglected as they represent second-order terms in volume fractions. Following the renormalization of Batchelor [5], the mean velocities of the particles relative to this mean motion of the system are then

$$u_3^{[1]} - u_3^{[fp]} = W^{[1]} - 5.5\phi^{[1]}W^{[1]} - \beta^{[12]}\phi^{[2]}W^{[2]} - \phi^{[1]}u_3^{[1]} - \phi^{[2]}u_3^{[2]}, \tag{B.5}$$

$$u_3^{[2]} - u_3^{[fp]} = W^{[2]} - 5.5\phi^{[2]}W^{[2]} - \beta^{[21]}\phi^{[1]}W^{[1]} - \phi^{[1]}u_3^{[1]} - \phi^{[2]}u_3^{[2]}, \tag{B.6}$$

where

$$\beta^{[12]} \equiv 1.5H^2 - 0.5 - 1.5f\left(H, \frac{R}{a^{[2]}}\right), \tag{B.7}$$

$$\beta^{[21]} \equiv 1.5H^2 - 0.5 - 1.5f\left(H, \frac{R}{a^{[1]}}\right), \tag{B.8}$$

The values of $\beta^{[12]}$ and $\beta^{[21]}$ are listed in table B1 for several different $H$ and $a^{[2]}/a^{[1]}$.

Several interesting observations can be made. After the mean flux of the system is subtracted out, the hindered settling of particles [5, 7] is recovered. The coefficient 5.5, in equations (B.5)

Table B1. The value of the coupling coefficients: the first value is $\beta^{[12]}$ and the second is $\beta^{[21]}$

| $a^{[2]}/a^{[1]}$ | 0.1 | 0.5 | 0.9 | 0.99 |
|---|---|---|---|---|
| $H = 10$ | 149.5, 4.233 | 25.35, 7.623 | 14.00, 11.65 | 12.86, 12.63 |
| $H = 20$ | 265.8, 5.175 | 32.36, 9.375 | 17.47, 14.46 | 16.00, 15.72 |
| $H = 30$ | 321.1, 5.726 | 36.46, 10.40 | 19.50, 16.10 | 17.84, 17.52 |
| $H = 50$ | 390.6, 6.422 | 41.63, 11.69 | 22.06, 18.18 | 20.17, 19.80 |
| $H = 100$ | 484.9, 7.365 | 48.65, 13.45 | 25.54, 20.99 | 23.32, 22.88 |

Table B2. Comparison of resulting sedimentation coefficients as defined in [7], for $H = 25$.

| $a^{[2]}/a^{[1]}$ | 0.1 | 0.5 | 0.9 | 0.99 |
|---|---|---|---|---|
| $S_{12}$, Eqn (B.10) | $-15.06$ | $-8.65$ | $-5.18$ | $-3.38$ |
| $S_{12}$, Batchelor and Wen [7] | $-5.29$ | $-4.29$ | $-3.83$ | $-3.68$ |
| $S_{21}$, Eqn (B.11) | $-18.97$ | $-39.76$ | $-112.5$ | $-366.5$ |
| $S_{21}$, Bactchelor and Wen [7] | $-5.95$ | $-9.81$ | $-24.32$ | $-78.53$ |

and (B.6), of the leading-order effect of aerodynamic interactions due to all other particles of same size compares reasonably well with Batchelor's exact result of 6.55 for Stokes disturbance flows [5, 7]. The difference is due to the non-exact treatment of the boundary conditions on the surface of particles in our superposition method.

The more interesting result is perhaps the effect of aerodynamic interactions due to the other-size particles, namely, the level of aerodynamic interactions in a bidisperse system. The coefficients listed in table B1 can be viewed as a measure of the magnitude of cross-size aerodynamic interactions. These coefficients are usually larger than 5.5 for the monodisperse system, due to the additional inaccessible region (i.e., shown as the gridded region in figure 3) caused by the non-overlap condition for unequal-size pairs [63]. If the AI truncation radius is made very large, the volume of this inaccessible region increases linearly with the truncation radius and the disturbance velocity decays as $1/r$, then the integral effect would imply that $\beta^{[12]}$ should linearly depend on $\ln(S^{[2]}/R)$. Indeed, when $S^{[2]} \gg R$, the asymptotic expression for $\beta^{[12]}$ is

$$\beta^{[12]} = \left[ 1.125 \ln \frac{2S^{[2]}}{R} + 1.3125 \right] \left( \frac{R}{a^{[2]}} \right)^2 - 0.625. \tag{B.9}$$

This explains why $\beta^{[12]}$ in table B1 continues to increase as $H$ is increased, when $a^{[2]}/a^{[1]}$ is close to one.

In table B2, we compare directly the bidisperse sedimentation coefficients resulting from equations (B.5) and (B.6), but using the definition of Batchelor and Wen [7],

$$S_{12} \equiv -\beta^{[12]} \times \left( \frac{a^{[2]}}{a^{[1]}} \right)^2, \tag{B.10}$$

$$S_{21} \equiv -\beta^{[21]} \times \left( \frac{a^{[1]}}{a^{[2]}} \right)^2. \tag{B.11}$$

Although the quantitative values differ from the exact values given in [7] due to the inexact treatment of the boundary conditions here [62], the qualitative behavior is nevertheless very similar. It is possible to improve the quantitative comparison here by adding lubrication effects of near-field interactions to our superposition method, following, for example, the methods of Revay and Higdon [50] and Dance and Maxey [23].

## References

[1] Aliseda, A., Cartellier, A., Hainaux, F. and Lasheras, J.C., 2002, Effect of preferential concentration on the settling velocity of heavy particles in homogeneous isotropic turbulence. *Journal of Fluid Mechanics*, **468**, 77–105.

[2] Allen, M.P. and Tildesley, D.J., 1987, *Computer Simulation of Liquids* (Oxford: Oxford University Press).

[3] Al-Naafa, M.A. and Sami Selim, M., 1992, Sedimentation of monodisperse and bidisperse hard-sphere colloidal suspensions. *AICHE Journal*, **38**, 1618–1630.

[4] Almeida, F.C. de, 1979, The collisional problem of cloud droplets moving in a turbulent environment: part II. Turbulent collision efficiencies. *Journal of Atmospheric Sciences*, **36**, 1564–1576.

[5] Batchelor, G.K., 1972, Sedimentation in a dilute dispersion of shperes. *Journal of Fluid Mechanics*, **52**, 245–268.

[6] Batchelor, G.K., 1982, Sedimentation in a dilute polydisperse system of interacting spheres: part 1. General theory. *Journal of Fluid Mechanics*, **119**, 379–408.

[7] Batchelor, G.K. and Wen, C.-S., 1982, Sedimentation in a dilute polydisperse system of interacting spheres: part 2. Numerical results. *Journal of Fluid Mechanics*, **124**, 495–528.

[8] Batchelor, G.K. and Janse van Rensburg, R.W., 1986, Structure formation in bidisperse sedimentation. *Journal of Fluid Mechanics*, **166**, 379.

[9] Brady, J.F. and Bossis, G., 1988, Stokesian dynamics, *Annual Review Fluid Mechanics*, **20**, 111–157.

[10] Brenner, M.P., 1999, Screening mechanisms in sedimentation. *Physics of Fluids*, **11**, 754–772.

[11] Bruneau, D., Anthore, R., Feuillebois, F., Auvray, X. and Petipas, C., 1990, measurement of average velocity of sedimentation in dilute polydisperse suspension of spheres. *Journal of Fluid Mechanics*, **221**, 577–596.

[12] Burton, T.M. and Eaton, J.K., 2002, Analysis of a fractional-step method on overset grids. *Journal of Computational Physics*, **177**, 336–364.

[13] Burton, T.M. and Eaton, J.K., 2002, High-resolution simulations of particle-eddy interactions. *Powder Technology*, **125**, 104–110.

[14] Buscall, R., Goodwin, J.W., Ottewill, R.H. and Tadros, T.F., 1982, The settling of particles through Newtonian and non-Newtonian media. *Journal of Colloid Interface Science*, **85**, 78–86.

[15] Caflisch, R.E. and Luke, J.H.C., 1985, Variance in the sedimentation speed of a suspension. *Physics of Fluids*, **28**, 759–760.

[16] Chun, J. and Koch, D.L., 2005, Coagulation of monodisperse aerosol particles by isotropic turbulence. *Physics of Fluids*, **17**, 027102.

[17] Chun, J., Koch, D., Rani, S.L., Ahluwalia, A. and Collins, L.R., 2005, Clustering of aerosol particles in isotropic turbulence. *Journal of Fluid Mechanics*, **536**, 219–251.

[18] Climent E. and Maxey, M.R., 2003, Numerical simulations of random suspensions at finite Reynolds numbers. *International Journal of Multiphase Flow*, **29**, 579–601.

[19] Climent E. and Maxey, M.R., 2004, Settling and instability of bidisperse suspensions. *5th International Conference on Multiphase Flow*, 30 May– 4 June 2004, Yokohama, Japan, paper no. 496.

[20] Collins, L.R. and Keswani, A., 2004, Reynolds number scaling of particle clustering in turbulent aerosols. *New Journal of Physics*, **6**, 119.

[21] Crowe, C.T., Sommerfeld, M. and Tsuji, Y., 1998, *Multiphase flows with droplets and particles*, Boca Raton, FL: CRC Press, p. 791.

[22] Cunha, F.R., Abade, G.C., Sousa, A.J. and Hinch, E.J., 2002, Modeling and direct simulation of velocity fluctuations and particle-velocity correlations in sedimentation. *Journal of Fluids Engineering*, **124**, 957–968.

[23] Dance, S.L. and Maxey, M.R., 2003, Incorporation of lubrication effects into the force-coupling method for particulate two-phase flow. *Journal of Computational Physics*, **189**, 212–238.

[24] R.H. Davis, 1984, The rate of coagulation of a dilute polydisperse system of sedimenting spheres, *Journal of Fluid Mechanics*, **145**, 179–199.

[25] Davis, R.H., 1996, Hydrodynamic diffusion of suspended particles: a symposium. *Journal of Fluid Mechanics*, **310**, 325–335.

[26] Davis, R.H. and Acrivos, A., 1985, Sedimentation of non-colloidal particles at low Reynolds numbers. *Annual Review of Fluid Mechanics*, **17**, 91–118.

[27] Davis, R.H. and Birdsell, K.H., 1988, Hindered settling of semidilute monodisperse and polydisperse suspensions. *AICHE Journal*, **34**, 123–129.

[28] Davis, R.H. and Gecol, H., 1994, Hindered settling function with no empirical parameters for polydisperse suspensions. *AICHE Journal*, **40**, 570–575.

[29] Eaton, J.K. and Fessler, J.R., 1994, Preferential concetration of particles by turbulence. *International Journal of Multiphase Flow*, **20**, 169–209.

[30] Elghobashi, S., 1994, On predicting particle-laden turbulent flows. *Applied Scientific Research*, **52**, 309–329.

[31] Eswaran, V. and Pope, S.B., 1988, An examination of forcing in direct numerical simulations of turbulence. *Computers and Fluids*, **16**, 257–278.

[32] Franklin, C.N., Vaillancourt, P.A., Yau, M.K. and Bartello, P., 2005, Collision rates of cloud droplets in turbulent flow. *Journal of Atmospheric Science*, **62**, 2451–2466.

[33] Grabowski, W.W. and Vaillancourt, P., 1999, Comments on "Preferential concentration of cloud droplets by turbulence: effects on the early evolution of cumulus cloud droplet spectra." *Journal of Atmospheric Science*, **56**, 1433–1436.

[34] Hinch, E.J., 1988, Sedimentation of small particles. In E. Guyon, J.-P. Nadal and Y. Pomeau (Eds.), *Disorder and Mixing* (Dordrecht: Kluwer) pp. 153–161.

[35] Hocking, L.M., 1973, Effect of slip on motion of a sphere close to a wall and of 2 adjacent spheres. *Journal of Engineering Mathematics*, **7**, 207–221.

[36] Jeffrey, D.J. and Onishi, Y., 1984, Calculation of the resistance and mobility functions for two unequal rigid spheres in low-Reynolds-number flow, *Journal of Fluid Mechanics*, **139**, 261–290.

[37] Kim, S. and Karrila, S.J., 1991, *Microhydrodynamics, Principles and Selected Applications*. Boston: Butterworth-Heinemann, p. 507.

[38] Koch, D.L. and Shaqfeh, E.S.G., 1991, Screening in sedimenting suspensions. *Journal of Fluid Mechanics*, **224**, 275–303.

[39] Koziol, A.S. and Leighton, H.G., 1996, The effect of turbulence on the collision rates of small cloud drops. *Journal of Atmospheric Science*, **53**, 1910–1920.

[40] Ladd, A.J.C., 1996, Hydrodynamic screening in sedimenting suspensions of non-Brownian spheres. *Physical Review Letters*, **76**, 1392–1395.

[41] Ladd, A.J.C., 1997, Sedimentation of homogeneous suspensions of non-Brownian spheres. *Physics of Fluids*, **9**, 491–499.

[42] Maxey, M.R., 1987, The gravitational settling of aerosol-particles in homogeneous turbulence and random flow fields. *Journal of Fluid Mechanics*, **174**, 441–465.

[43] Mucha, P.J., Tee, S.Y., Weitz, D.A., Shraiman, B.I. and Brenner, M.P., 2004, A model for velocity fluctuations in sedimentation. *Journal of Fluid Mechanics*, **501**, 71–104.

[44] Nicolai, H., Herzhaft, B., Hinch, E.J., Oger, L. and Guazelli, E., 1995, Particle velocity fluctuations and hydrodynamic self-diffusion of sedimenting non-Brownian spheres. *Physics of Fluids*, **7**, 12–23.

[45] Noh Y. and Fernando, H.J.S., 1993, The transition in the sedimentation pattern of a particle cloud. *Physics of Fluids*, **5**, 3049–3055.

[46] Peysson, Y. and Guazzelli, E., 1999, Verlocity fluctuations in a bidisperse sedimenting suspension. *Physics of Fluids*, **11**, 1953–1955

[47] Pinsky, M.B., Khain, A.P. and Shapiro, M., 1999, Collision of small drops in a turbulent flow. Part I. Collision efficiency, Problem formulation and preliminary results. *Journal of Atmospheric Sciences*, **56**, 2585–2600.

[48] Pruppacher, H.R. and Klett, J.D., 1997, *Microphysics of Clouds and Precipitation*, 2nd edition, Boston: Kluwer, p. 954.

[49] Ramaswamy, S., 2001, Issues in the statistical mechanics of steady sedimentation. *Advances in Physics*, **50**, 297-341.

[50] Revay, J.M. and Higdon, J.J.L., 1992, Numerical simulation of polydisperse sedimentation: equal size spheres. *Journal of Fluid Mechanics*, **243**, 15.

[51] Richardson, J.F. and Zaki, W.N., 1954, Sedimentation and fluidization: part I. *Transactions of Institution of Chemical Engineers*, **32**, 35–53.

[52] Seinfeld, J.H. and S.N. Pandis, 1997, *Atmospheric Chemistry and Physics: From Air Pollution to Climate Change*. (New York: Wiley).

[53] Schulze, H.J., 1984, *Physico-Chemical Elementary Proceses in Flotation*. Amsterdam: Elsevier.

[54] Segre, P.N., Herbolzheimer, E., Chaikin, P.M., 1997, Long-range correlations in sedimentation. *Physical Review Letters*, **79**, 2574-2577.

[55] Smook, G.A., 1982, *Handbook for Pulp anf Paper Technologists*. Montreal: Canadian Pulp and Paper Association.

[56] Squires, K.D. and Eaton, J.K., 1991, Preferential concentration of particles by turbulence. *Physical Fluids* A **3**, 1169–1178.

[57] Sundaram, S. and Collins, L.R., 1997, Collision Statistics in an Isotropic, Particle-Laden Turbulent Suspension. *Journal of Fluid Mechanics*, **335**, 75–109.

[58] Sundararajakumar, R.R. and Koch, D.L., 1996, Non-continuum lubrication flows between particles colliding in a gas. *Journal of Fluid Mechanics*, **313**, 283–308.

[59] Tory, E.M., 1996, *Sedimentation of Small Particles in a Viscous Fluid*. South Hampton, UK: Computational Mechanics Publications, p. 281.

[60] Wang, L.-P. and Maxey, M.R., 1993, Settling velocity and concentration distribution of heavy particles in homogeneous isotropic turbulence. *Journal of Fluid Mechanics*, **256**, 27–68.

[61] Wang, L.-P., Wexler, A.S. and Zhou, Y., 2000, Statistical Mechanical Descriptions of Turbulent Coagulation of Inertial Particles. *Journal of Fluid Mechanics*, **415**, 117–153.

[62] Wang, L.-P., Ayala, O. and Grabowski, W.W., 2005a, Improved formulations of the superposition method. *Journal of Atmospheric Sciences*, **62**, 1255–1266.

[63] Wang, L.-P., Ayala, O., Kasprzak, S.E. and Grabowski, W.W., 2005b, Theoretical formulation of collision rate and collision efficiency of hydrodynamically-interacting cloud droplets in turbulent atmospheres. *Journal of Atmospheric Sciences*, **62**, 2433–2450.

[64] Wang, L.P., Xue, Y., Ayala, O. and Grabowski, W.W., 2005c, Effects of stochastic coalescence and air turbulence on the size distribution of cloud droplets. *Atmospheric Research*, **82**, 416–432.

[65] Wang, L.-P., Franklin, C.N., Ayala, O. and Grabowski, W.W., 2005d, On probability distributions of angle-of-approach and relative velocity of colliding droplets in a turbulent flow. *Journal of Atmospheric Sciences*, **63**, 881–900.

[66] Yang, T.S. and Shy, S.S., 2003, The settling velocity of heavy particles in an aqueous near-isotropic turbulence. *Physics of Fluids*, **15**, 868–880.

[67] Yang, T.S. and Shy, S.S., 2005, Two-way interaction between solid particles and homogeneous air turbulence: particle settling rate and turbulence modification measurements. *Journal of Fluid Mechanics*, **526**, 171–216.

[68] Zhou, Y., Wexler, A.S. and Wang, L.-P., 1998, On the collision rate of small particles in isotropic turbulence. Part 2. Finite-inertia case. *Physics of Fluids*, **10**, 1206–1216.

[69] Zhou, Y., Wexler, A.S. and Wang, L.-P., 2001, Modelling turbulent collision of bidisperse inertial particles. *Journal of Fluid Mechanics*, **433**, 77–104.